

Seismic diffraction imaging to characterise mass-transport complexes: examples from the Gulf of Cadiz, south west Iberian Margin

This manuscript is a non-peer reviewed pre-print submitted to EarthArXiv. The manuscript has been submitted for publication in Journal of Geophysical Research: Solid Earth. If accepted, the final version of this manuscript will be available via the Peer-reviewed Publication DOI link on the right-hand side of this webpage.

Please feel free to contact any of the authors, we welcome feedback:

Jonathan Ford^{1,2} (jford@inogs.it)

Roger Urgeles³ (urgeles@icm.csic.es)

Angelo Camerlenghi¹ (acamerlenghi@inogs.it)

Eulàlia Gràcia³ (egracia@icm.csic.es)

¹National Institute of Oceanography and Applied Geophysics (OGS)

²University of Trieste

³Institut de Ciències del Mar (CSIC)

1 **Seismic diffraction imaging to characterise**
2 **mass-transport complexes: examples from the Gulf of**
3 **Cadiz, south west Iberian Margin**

4 **Jonathan Ford^{1,2}, Roger Urgeles³, Angelo Camerlenghi¹, Eulàlia Gràcia³**

5 ¹National Institute of Oceanography and Applied Geophysics - OGS

6 ²University of Trieste

7 ³Institut de Ciències del Mar, CSIC

8 **Key Points:**

- 9 • Seismic diffractions encode information about the small-scale internal structure
10 of mass-transport complexes (MTCs)
- 11 • Diffraction images offer a low-cost route to improve the lateral resolution and ef-
12 fective vertical resolution of seismic images of MTCs
- 13 • The superior illumination of out-of-plane diffractions means that 2-D seismic pro-
14 files encode information about the 3-D structure of MTCs

Corresponding author: Jonathan Ford, jford@inogs.it

Abstract

Mass-transport complexes (MTCs) are often characterised by small-scale, discontinuous internal structure, such as included blocks, rough interfaces, faults and truncated strata. Seismic reflections are fundamentally limited in lateral resolution by the source bandwidth, meaning that seismic images may not properly image such structure. The relatively weak seismic diffractions, instead, encode information on sub-wavelength scale structure with superior illumination. In this paper, we compare diffraction imaging to conventional, full-wavefield seismic imaging to characterise MTCs. We apply a seismic diffraction imaging workflow based on plane-wave destruction filters to two 2-D marine multi-channel seismic profiles from the Gulf of Cadiz. We observe that MTCs generate a large amount of diffracted energy relative to the unfailed confining sediments. The diffraction images show that some of this energy is localised along existing discontinuities imaged by the full-wavefield images. We demonstrate that, in combination with full-wavefield images, diffraction images can better discriminate the lateral extent of MTCs, particularly for thin bodies. We suggest that diffraction images may be a more physically correct alternative to seismic discontinuity attributes derived from full-wavefield images. Finally, we outline a speculative approach to utilise the out-of-plane diffractions generated by the 3-D structure of MTCs, normally considered a nuisance in 2-D seismic processing. We use a controlled synthetic test and a real data example to show that under certain conditions these out-of-plane diffractions might be used to constrain the minimum width of MTCs from single 2-D seismic profiles.

Plain Language Summary

Underwater landslides are a significant geohazard that can generate large magnitude tsunamis and threaten seafloor infrastructure such as pipelines and telecommunication cables. The deposits from these events (so-called mass-transport complexes, or MTCs) can preserve internal structure that can reveal the dynamics of failure, important to understand the geohazard potential from future events. One common tool for investigating these deposits is seismic imaging, which uses recordings of seismic waves reflected and scattered from the subsurface to image the geology. The resolution of the reflected waves is often too poor to properly characterise the complex, strongly deformed internal structure of MTCs. In this study, we instead use the seismic waves scattered at lateral, basal and internal discontinuities formed by landslide processes to produce diffrac-

47 tion images of MTCs. We show that these images have improved resolution and illumi-
48 nation of the small-scale structure. We suggest that diffraction imaging could be a use-
49 ful tool for geohazard investigations of complex geology.

50 1 Introduction

51 Mass-transport complexes (MTCs) are the deposits of subaqueous mass-movements
52 such as debris flows, slides and slumps (Prior et al., 1984; Mulder & Cochonat, 1996; Piper
53 et al., 1997; Sawyer et al., 2009). Subaqueous mass-movements pose a significant geo-
54 hazard to coastal populations from landslide-induced tsunami (Tappin et al., 2001; Sa-
55 take, 2012) and to seafloor infrastructure such as telecommunications cables and pipelines
56 (Piper et al., 1999; Carter et al., 2014). MTCs have important implications for hydro-
57 carbon exploration as they form a significant proportion of deep-water sediment fill (Weimer
58 & Shipp, 2004) and they can have both reservoir and seal potential (Alves et al., 2014;
59 Cardona et al., 2016). They also represent a drilling hazard as they are often over-consolidated
60 (densified) compared to unfailed sediments (Shipp et al., 2004).

61 MTCs can preserve complex, laterally discontinuous internal structure such as in-
62 cluded blocks, rough interfaces, faults and truncated strata (Lucente & Pini, 2003; Bull
63 et al., 2009). These so-called *kinematic indicators* can record the dynamics of failure,
64 transport and emplacement, important for constraining the flow type and the geohaz-
65 ard potential of future mass-movements. When the scale of this structure is close to the
66 limit of seismic resolution, seismic images of MTCs can be difficult to interpret, often
67 showing an apparently “chaotic” or “disordered” seismic character (Posamentier & Mar-
68 tinsen, 2011). This can be a problem when discriminating between different types of mass-
69 movements, for example debris flow deposits (lacking internal bedding, chaotic seismic
70 character) and slumps (internal bedding preserved but may still show a chaotic seismic
71 character without sufficient seismic resolution). It can also be difficult to characterise
72 the amount and style of deformation within a deposit.

73 Efforts to improve the characterisation of internal structure from seismic images
74 have largely relied on improvements in seismic acquisition technology in recent decades.
75 Industry-scale 3-D seismic surveys can provide the spatial resolution and coverage to ob-
76 serve large-scale internal structure within MTCs, particularly from plan-view time and
77 depth slices (e.g., Frey Martinez et al., 2005; Bull et al., 2009; Gafeira et al., 2010; Lackey

78 et al., 2018; Steventon et al., 2019). In academic settings maximum offsets are typically
79 short relative to the target depth, meaning reflectors are often poorly illuminated, in-
80 trinsically limiting the lateral resolution. Improvements in imaging of academic data have
81 typically come from novel acquisition geometries and seismic sources, such as ultra-high
82 resolution deep-tow seismic (Badhani et al., 2020) and short-offset 3-D “P-cable”-type
83 geometries (Berndt et al., 2012; Karstens et al., 2019). Such approaches can provide dra-
84 matic increases in seismic resolution within MTCs at the cost of increased acquisition
85 effort.

86 An alternative strategy to improve the interpretable resolution of existing seismic
87 data is to apply quantitative interpretation techniques such as seismic attributes (Chopra
88 & Marfurt, 2007). Seismic attributes can highlight discontinuities and identify areas of
89 disrupted seismic reflectors by deriving statistical properties within data windows of seis-
90 mic images. Such approaches have been applied to discriminate MTCs from background
91 sedimentation (when they have chaotic internal seismic character) and characterise the
92 flow direction and assess the degree of internal disaggregation (e.g., Alves et al., 2014;
93 Bhatnagar et al., 2019). Seismic attributes, however, are typically derived from full-wavefield
94 seismic images, which suffer from the lateral resolution limits outlined above, and data
95 windowing can reduce their effective resolution in comparison to the original image.

96 Conventional seismic processing emphasises preserving and imaging the reflected
97 seismic wavefield — the relatively weak diffracted wavefield is often ignored, aliased or
98 accidentally attenuated (Klem-Musatov et al., 2016; Schwarz, 2019b). Seismic reflections
99 cannot properly resolve geological structures smaller than the Rayleigh limit (i.e., half
100 a seismic wavelength; on the order of metres to decametres for marine airgun data) (Born
101 & Wolf, 1959; Chen & Schuster, 1999). Such structures, instead, scatter the seismic waves
102 and generate diffractions, meaning that the diffracted wavefield can encode sub-wavelength
103 information about small-scale subsurface discontinuities. Contrary to reflections, the ra-
104 diation pattern of diffractions is independent of the dip (Fig. 1), meaning that they can
105 be fully illuminated even by short- or zero-offset receiver arrays (Preine et al., 2020).

106 Diffraction imaging works by separating the reflected and diffracted wavefields and
107 migrating only the diffracted component, producing an image of the small-scale, sub-wavelength
108 heterogeneous subsurface (Klem-Musatov et al., 2016; Schwarz, 2019b). Several approaches
109 for diffraction separation have been developed. Some exploit the difference in moveout

110 of reflections and diffractions in common-shot or common-midpoint domains (Khaidukov
111 et al., 2004), or the difference in dip and lateral continuity between reflections and diffrac-
112 tions in common-offset domain (Taner et al., 2006; Fomel et al., 2007; Decker et al., 2017).
113 Others rely on wavefront attributes and the assumed coherence of seismic reflections to
114 model and subtract the reflected wavefield (Dell & Gajewski, 2011; Schwarz & Gajew-
115 ski, 2017). Another approach is to perform the separation during migration, exploiting
116 the fact that in migrated dip-angle domain diffractions appear flat, whereas reflections
117 appear as hyperbolae (Moser & Howard, 2008). Even if diffractions are properly preserved
118 during processing, they may still be masked by the relatively high amplitude, low res-
119 olution and long wavelength seismic reflections. Diffraction imaging therefore offers po-
120 tentially higher lateral resolution and better illumination of small-scale, discontinuous
121 geological structure compared to conventional full-wavefield seismic images.

122 MTCs very often contain a large amount of *diffraction generators*: interfaces with
123 width below the Rayleigh criterion (sub-wavelength scale heterogeneities) or near-infinite
124 local curvature (edges, discontinuities and truncations) (Fig. 1a). Examples of such struc-
125 ture could include the hinges of slump folds (Alsop & Marco, 2013); offset across nor-
126 mal and reverse faults within extensional and compressional shear zones (Posamentier
127 & Martinsen, 2011); wavelength-scale transported clasts (Talling et al., 2010); truncated
128 reflectors at the boundaries of slide blocks (Sobiesiak et al., 2016); rough basal topog-
129 raphy and ramp-and-flat structures (Lucente & Pini, 2003); headwall scarps (Bull et al.,
130 2009) and steep, erosive lateral margins (Frey Martinez et al., 2005) (Fig. 1b). This points
131 to the potential of seismic diffractions to encode unique information on the small-scale
132 internal structure and the discontinuous external boundaries of MTCs. Indeed, the pres-
133 ence of diffraction tails (sometimes referred to as *hyperbolae*, although diffractions are
134 only strictly hyperbolic when the overburden velocity structure is laterally homogenous)
135 in unmigrated seismic and sub-bottom profiles is often used as an indicator of mass-movements
136 (Urgeles et al., 1999; Diviacco et al., 2006). Even MTCs that do preserve coherent, well-
137 imaged internal strata or internal geometry may benefit from the superior illumination
138 of diffractions, especially at the discontinuous basal surface, lateral margins and inter-
139 nal dislocation planes between slide blocks. Structural reconstruction to quantify strain
140 distribution within MTCs relies on the proper imaging of such supra-seismic scale in-
141 terfaces (Steventon et al., 2019; Bull & Cartwright, 2020).

142 Seismic diffraction imaging has been used to characterise a range of complex ge-
143 ological targets including faults, channels, pinchouts, rugose interfaces, karstic carbon-
144 ate reservoirs and fracture zones (Fomel et al., 2007; Reshef & Landa, 2009; Decker et
145 al., 2015). In this paper we explore the potential of diffraction imaging to characterise
146 the complex internal structure and external morphology of MTCs. This approach has
147 the potential to increase the value of existing seismic data during processing at relatively
148 low additional computational cost. We apply diffraction imaging to two 2-D, multi-channel
149 seismic profiles containing prominent MTCs from the Gulf of Cadiz (south west Iberian
150 Margin). We first demonstrate the ability of diffraction images to resolve small-scale in-
151 ternal structure compared to conventional full-wavefield seismic images. We then com-
152 pare diffraction images to traditional seismic discontinuity attributes for identification
153 and interpretation of relatively small, thin MTCs. Finally, we outline a speculative ap-
154 proach to utilise the illumination of out-of-plane diffractions (normally considered a nui-
155 sance) and the inherently 3-D structure of MTCs. We suggest that in certain conditions
156 this out-of-plane diffracted energy might be used to constrain the minimum cross-line
157 width of MTCs from single 2-D seismic profiles.

158 **2 Geological Setting**

159 The Gulf of Cadiz is located offshore the south west margin of the Iberian Penin-
160 sula and north west Morocco (Fig. 2). The region is characterised by active tectonics re-
161 lated to convergence between the African and Eurasian plates. The tectonic structure
162 and seafloor morphology of the gulf is the result of an accretionary wedge formed from
163 the Late Cretaceous to the Late Miocene (Zitellini et al., 2009). The accretionary wedge
164 is covered by Late Miocene to Plio-Quaternary sediments, pierced by mud volcanoes and
165 pockmarks (indicating active fluid flow) and salt diapirs (Gràcia, Dañobeitia, Vergés, Bar-
166 tololomé, & Córdoba, 2003; Gràcia, Dañobeitia, Vergés, & Team, 2003; Zitellini et al., 2009;
167 Medialdea et al., 2009). The Gulf of Cadiz and the south west Iberian Margin host large
168 magnitude ($M_w > 8$) earthquakes (Gràcia et al., 2010; Matias et al., 2013) and sub-
169 marine landslides (Urgeles & Camerlenghi, 2013). Both processes pose significant tsunami
170 hazard to nearby coastal populations (Baptista & Miranda, 2009; Lo Iacono et al., 2012;
171 Leynaud et al., 2017). This study uses geophysical data collected from two areas of the
172 Gulf of Cadiz: the Portimão Bank and the Infante Don Henrique Basin.

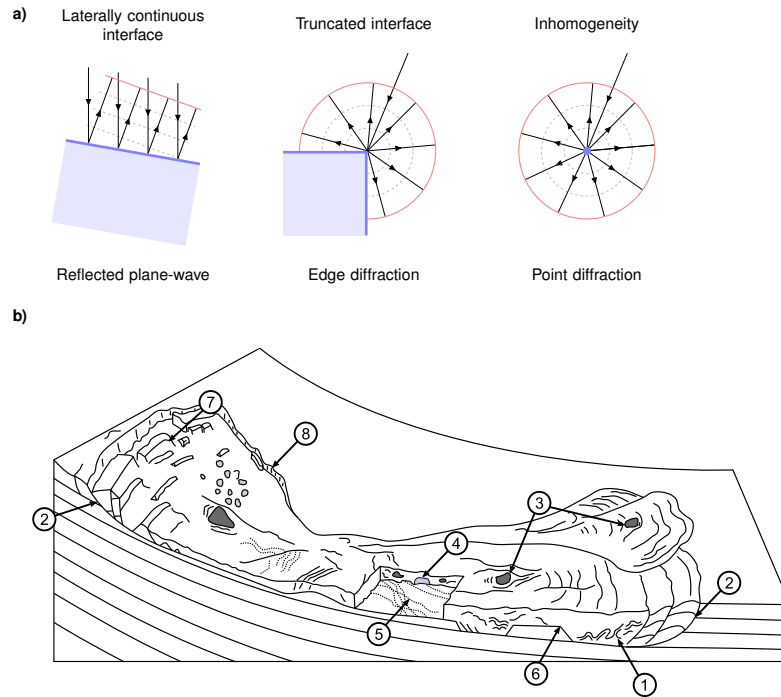


Figure 1. a) The 2-D radiation pattern of reflections from a laterally continuous interface compared to diffractions from truncations (infinite curvature *edge diffractors*) or sub-wavelength scale heterogeneities (*point diffractors*). b) Schematic diagram of an MTC labelled with discontinuous structure likely to generate seismic diffractions: 1) intense folding; 2) extensional and compressional shear zones; 3) transported clasts; 4) boundaries of slide blocks; 5) rough basal topography; 6) ramp-and-flat structures; 7) headwall scarps and 8) lateral margins (modified from Bull et al., 2009).

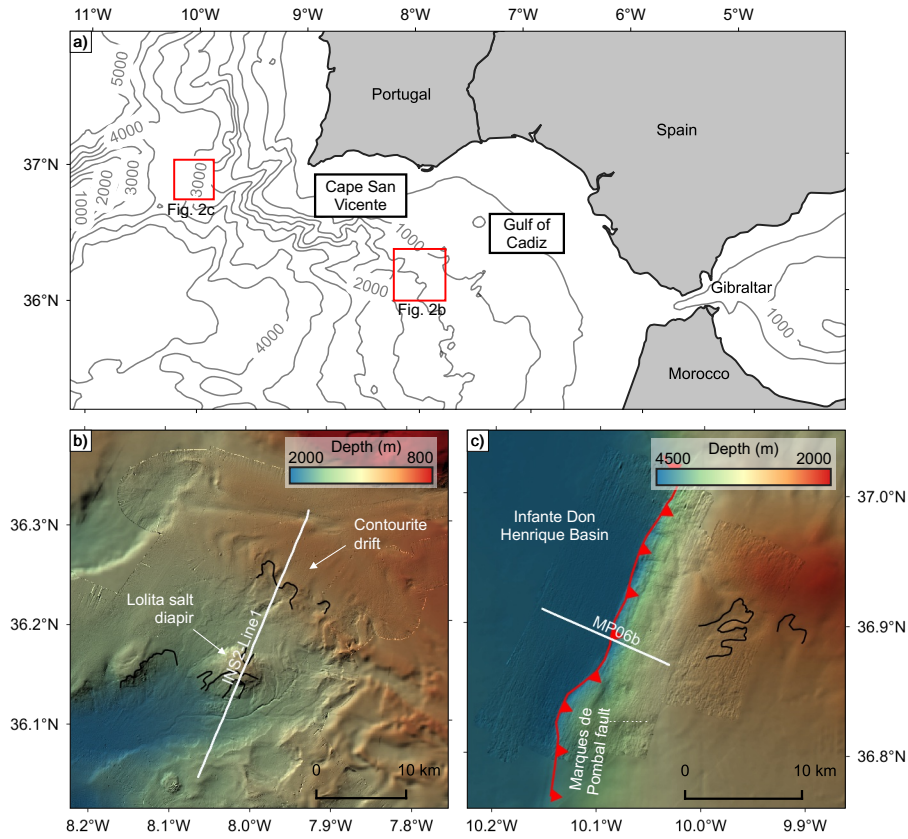


Figure 2. a) Overview map of the Gulf of Cadiz and surroundings, with bathymetric contours (500 m interval). b) Bathymetry of Portimão Bank area, location of seismic profile INS2-Line1 indicated. c) Bathymetry of Infante Don Henrique Basin area, location of Marquês de Pombal fault trace at the seafloor (after Gràcia, Dañobeitia, Vergés, & Team, 2003) and seismic profile MP06b indicated. Headscarps from mass-movements are shown as black lines.

173 The Portimão Bank is an east-west trending tectonic high located south of Por-
174 tugal, at the external part of the Gulf of Cadiz. The area is characterised by bottom cur-
175 rents and contourite deposition associated with the Mediterranean Outflow Water (Brackenridge
176 et al., 2013) and mass-movements (slides and slide scars; Silva et al., 2020). Salt diapirs
177 pierce the shallow Plio-Quaternary sediments and the corresponding doming is evident
178 in the bathymetry (Fig. 2). The rapid deposition of poorly consolidated contourites and
179 slope steepening from salt diapirism are primary pre-conditioning factors for mass-failure,
180 evidence of which is widespread in the area (Mulder et al., 2009; Silva et al., 2020).

181 The Infante Don Henrique Basin is located at the south west of the Cape São Vi-
182 cente (Fig. 2). It is bound on its eastern side by the Marquês de Pombal fault, an ap-
183 proximately 55 km long, north-south trending, active reverse thrust fault (Gràcia, Dañoibeitia,
184 Vergés, Bartolomé, & Córdoba, 2003; Terrinha et al., 2003; Zitellini et al., 2004). The
185 fault is expressed in the bathymetry as a monocline, with water depth rapidly increas-
186 ing from the hanging-wall block (2000 m water depth) to the basin located in the foot-
187 wall block (3900 m water depth). A succession of stacked MTCs is preserved in the Plio-
188 Quaternary deposits in the basin, likely recording recent seismic activity of the fault (Vizcaino
189 et al., 2006; Gràcia et al., 2010). Recent mass-failure events are also visible in the bathymetry
190 of the steeply dipping hanging wall block (Fig. 2c). The Marquês de Pombal fault has
191 been considered as a potential source of the $M_w > 8$ 1755 Lisbon earthquake (Baptista
192 et al., 1998; Terrinha et al., 2003). Preconditioning factors for mass-failure in the area
193 include slope steepening of the advancing thrust front and potential excess pore pres-
194 sure related to the relatively high sedimentation rate and lateral fluid flow. Near-field
195 seismic activity along the Marquês de Pombal fault is likely a primary trigger mecha-
196 nism for some of the mass-failure events, as well as far-field seismicity from the rest of
197 the Gulf of Cadiz.

198 **3 Data and Methods**

199 **3.1 Geophysical Data**

200 This study uses two 2-D marine multi-channel seismic reflection profiles from the
201 Gulf of Cadiz acquired during the INSIGHT (Imaging large seismogenic and tsunamigenic
202 structures of the Gulf of Cadiz with ultra-high resolution technologies) cruises in May
203 2018 (Leg 1) and October 2019 (Leg 2) (Gràcia et al., 2018; Urgeles et al., 2019).

204 The seismic acquisition and processing flow were designed to maximise the tem-
205 poral and spatial resolution of the resulting seismic images. The shot interval was cho-
206 sen to ensure a nominal coverage of at least 12-fold with a midpoint interval of 3.125 m.
207 A relatively small seismic source (an airgun array with total volume 930 cu. in.) was used
208 to maximise the dominant source frequency. The source array and streamer were towed
209 at a relatively shallow depth (approximately 3 m) to ensure that the frequency of the first
210 source and receiver ghost notches was as high as possible. Broadband pre-processing was
211 performed onboard using RadExPro seismic processing software. Traditional pre-processing
212 focuses on imaging specular reflections, meaning that diffractions are often ignored or
213 removed. Preserving diffractions through the pre-processing flow requires care as they
214 are generally lower amplitude, higher frequency and dip more steeply compared to re-
215 flections. The broadband pre-processing flow consisted of i) swell noise removal (to en-
216 hance the signal-to-noise ratio at low frequencies); ii) deghosting (to correct for the source
217 and receiver ghost effect, enhancing the bandwidth); iii) designature (to transform the
218 data to zero-phase and remove the bubble pulse, boosting the low frequency content) and
219 iv) shot domain $\tau - p$ muting (to remove steeply dipping noise). For most of the sur-
220 vey area the signal penetration depth was similar to or less than the two-way travel time
221 (TWTT) of the first waterbottom multiple, therefore no multiple attenuation was per-
222 formed. Instead, a bottom-mute was applied from above the first waterbottom multi-
223 ple before imaging to prevent high amplitude multiple energy from migrating upwards
224 into the shallow section as noise. Full details of the acquisition and pre-processing pa-
225 rameters for both profiles are given in the supplementary information (Table S1 and Ta-
226 ble S2). The signal bandwidth of the migrated full-wavefield images is approximately 8 Hz
227 to 250 Hz (range estimated from the amplitude spectrum of a window around the wa-
228 terbottom reflection, 20 dB below the peak amplitude).

229 3.2 Diffraction Separation

230 This study uses a data domain, dip-guided plane-wave destruction (PWD) filter
231 approach for diffraction separation, modified to be robust to high amplitude diffractions
232 and steeply dipping reflections present in the example profiles from the Gulf of Cadiz.
233 Fig. 3 shows an outline of the diffraction imaging workflow compared to a conventional
234 full-wavefield seismic imaging workflow.

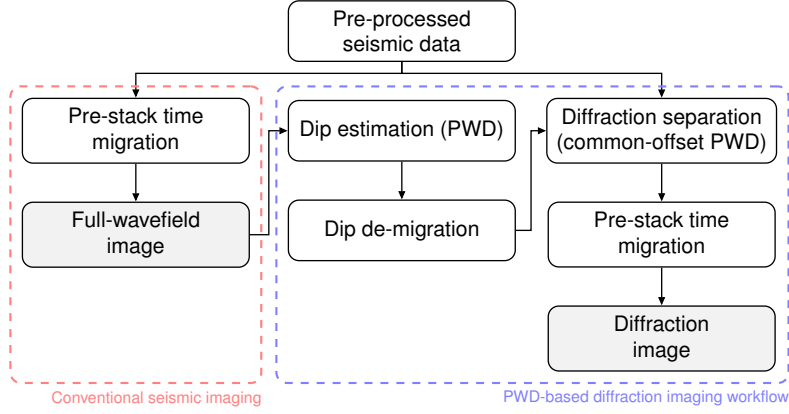


Figure 3. Comparison of workflows for conventional full-wavefield seismic imaging and the plane-wave destruction (PWD) filter based diffraction separation and imaging workflow used in this study. The dip field is estimated from the migrated full-wavefield image, then de-migrated using the migration velocities giving the dominant slope of the unmigrated reflections (Appendix A). This is used to guide the PWD filter for diffraction separation.

235 The recorded seismic wavefield is composed of i) reflected energy, ii) diffracted en-
 236 ergy and iii) noise (including other seismic arrivals, such as multiples). When the noise
 237 is low, the diffracted wavefield can be retrieved by subtracting the reflected wavefield from
 238 the recorded wavefield. In this study we perform the separation using a dip-guided PWD
 239 filter approach in the time domain on common-offset gathers (as in, e.g., Fomel et al.,
 240 2007; Decker et al., 2017). This approach exploits the fact that reflections are locally pla-
 241 nar events in common-offset sections (Harlan et al., 1984). PWD filters calculate the dom-
 242 inant local slope by following energy between traces and iteratively minimising the resid-
 243 ual energy (Claerbout, 1992; Fomel, 2002). The residual energy contains the diffracted
 244 energy and noise, with laterally coherent events with continuous local slope (i.e., smooth)
 245 that are close to the estimated dominant slope (the apparent dip of the unmigrated re-
 246 flectors) eliminated.

247 The PWD filter is guided by an estimate of the dominant slope (dip). Robust diffrac-
 248 tion separation therefore depends on accurate estimation of the dominant slope of the
 249 *unmigrated* reflections. Due to the general rough topography of the seafloor in the Gulf
 250 of Cadiz, the example profiles in this study contain a large number of high energy diffrac-
 251 tions with similar amplitude to major reflections. In addition, some reflections are steeply

dipping, often sub-parallel to the diffraction tails. This prevents accurate estimation of the dominant slope of the reflectors directly from the unmigrated data as in, for example, Fomel et al. (2007). We instead estimate the dip field from the migrated full-wavefield image (i.e., where diffractions are collapsed and the continuity of reflections enhanced), then de-migrate this dip field using the migration velocities to estimate the dominant slope of the unmigrated reflections. Details of the dip de-migration algorithm are given in Appendix A.

3.3 Imaging

Diffractions, like reflections, can be imaged by Kirchhoff-type migrations, in both time and depth domains (Moser & Howard, 2008). For this study, the real data examples are migrated using a 2-D pre-stack Kirchhoff time migration (Lumley et al., 1994; Fomel et al., 2013), with a migration aperture limited to 60° . Identical migrations are performed for the full-wavefield and diffraction images so that the geometry of both images is comparable (Fig. 3). The diffraction images in this study are presented as the energy (squared envelope) of the diffraction image (as in, e.g., Preine et al., 2020).

A classic application for diffraction imaging is to derive migration velocity fields by focusing analysis of the diffracted wavefield (e.g., Fomel et al., 2007; Decker et al., 2017; Preine et al., 2020). Under the correct migration velocity, diffractions will collapse (focus) to a point at their apex. The example 2-D profiles in this study both contain significant contributions from out-of-plane diffractions around the target MTCs and from the rugose seafloor (Section 3.4). Out-of-plane diffractions will not be properly focused by 2-D migration, so their presence biases the derived migration velocity fields. As a consequence, we were not able to obtain plausible migration velocities from focusing-defocusing analysis of the diffracted wavefield in these examples.

A more traditional method for migration velocity analysis is to pick velocity trends from semblance panels of migrated common-midpoint gathers. This method relies on the approximately hyperbolic moveout of seismic reflections with offset. The example 2-D profiles in this study were acquired with a relatively short streamer, giving a low far-offset (hundreds of metres) with respect to the depth of the target MTCs (kilometres). Consequently, there was not great enough differential moveout between reflections to perform an accurate and robust semblance velocity analysis.

283 Instead, the migration velocity fields used in this study were derived during onboard
 284 processing as a constant velocity in the water column and a velocity gradient in the sed-
 285 iments. The post-migration waterbottom horizon was picked on a near-offset section mi-
 286 grated with a water velocity $f - k$ migration (Stolt, 1978). The optimal sediment ve-
 287 locity gradients were estimated for each area by generating an ensemble of images mi-
 288 grated with a range of gradients and choosing the gradient that appeared to best focus
 289 reflections and diffractions for all profiles in an area. The sediment velocity gradient is
 290 then inserted below the smoothed post-migration waterbottom horizon to make the mi-
 291 gration velocity field. For seismic profiles INS2-Line1 and MP06b the optimal sediment
 292 velocity gradient was estimated during onboard processing as 200 ms^{-2} and 125 ms^{-2} ,
 293 respectively (Gràcia et al., 2018; Urgeles et al., 2019). The water velocity for both pro-
 294 files is 1500 ms^{-1} . The resulting migration velocity fields are presented in the supplemen-
 295 tary information (Fig. S5). These migration velocities are considered reasonable at the
 296 target depths because the MTCs in these examples are close to the seafloor (with respect
 297 to the water depth) and both the reflection and diffraction images appear to be gener-
 298 ally well-focused. A sensitivity analysis of the diffraction imaging to changing the mi-
 299 gration velocities is presented in the supplementary information (Fig. S7).

300 **3.4 Constraining the Location of Out-of-Plane Diffractors**

301 For 2-D seismic profiles, out-of-plane energy (i.e., seismic energy reflected and scat-
 302 tered from interfaces outside the vertical plane of the profile) can contaminate the im-
 303 age. The illumination of seismic reflectors depends on the local dip of the reflector and
 304 the geometry of the receiver array. Diffractions, however, are 3-D phenomena, fully il-
 305 luminated from all angles even by single-channel, zero-offset data (Fig. 1a, Preine et al.,
 306 2020). This means that 2-D diffraction images will suffer more strongly from out-of-plane
 307 energy than corresponding 2-D reflection images. Out-of-plane energy is usually regarded
 308 as a source of noise in 2-D seismic profiles, as it cannot be properly migrated and inter-
 309 ferres with in-plane primary energy.

310 We suggest that these out-of-plane diffractions, under certain strong assumptions,
 311 may provide a source of information about the 3-D geology of MTCs from 2-D profiles.
 312 MTCs are inherently 3-D geobodies (Fig. 1b), so 2-D seismic images of MTCs will, in
 313 general, suffer more strongly from out-of-plane energy than 2-D seismic images of un-

314 failed sediments. Therefore we expect *diffraction images* of MTCs from 2-D seismic pro-
 315 files to contain particularly large contributions from out-of-plane energy.

316 The apparent TWTT of an out-of-plane diffractor, t_{diff} , can be predicted from
 317 the cross-line distance to the diffractor, x , the depth of the diffractor below the seismic
 318 datum, z , and the average velocity along the raypath from the seismic array to the diffrac-
 319 tor, v_{rms} (Fig. 4):

$$t_{diff} = \frac{2\sqrt{x^2 + z^2}}{v_{rms}}. \quad (1)$$

320 If diffractors are distributed throughout the MTC, some of the recorded diffrac-
 321 tion energy will always come from *outside* the vertical plane of the profile (i.e., $|x| >$
 322 0 in Fig. 4). If the body is wider than it is thick and contains abundant diffractors, the
 323 apparent thickness of the slide from diffraction images will be greater than the appar-
 324 ent thickness of the slide from reflection images. This results in a “shadow” of diffrac-
 325 tion energy below the true basal surface of the MTC in 2-D diffraction images. From Eq. 1
 326 it follows that the thickness of this *diffraction shadow* is related to the half-width, per-
 327 pendicular to the profile, of the zone of out-of-plane diffractors that contribute to the
 328 image. We propose that this could provide a minimum bound on the cross-line half-width
 329 of an MTC under certain (strong) assumptions:

330 **Diffractors spread throughout body** To relate the zone where out-of-plane diffrac-
 331 tions could potentially come from to the width of an MTC we need to assume that
 332 diffractors are spread throughout the body.

333 **Thin body** The thickness of the body is small relative to its depth, meaning that all
 334 diffractors can be treated as if they are at the top surface.

335 **Laterally homogeneous overburden velocity** Eq. 1 assumes a straight raypath to
 336 the true location of the diffractor, implying that the overburden velocity, v_{rms} ,
 337 is constant in a cross-line direction, even if the water depth changes.

338 **Clear diffraction shadow** The diffraction shadow is associated with a single body and
 339 can be clearly differentiated from the background and from other bodies that might
 340 also generate diffractions. The cross-line width is large enough with respect to the
 341 thickness that the diffraction shadow extends *below* the true basal reflector.

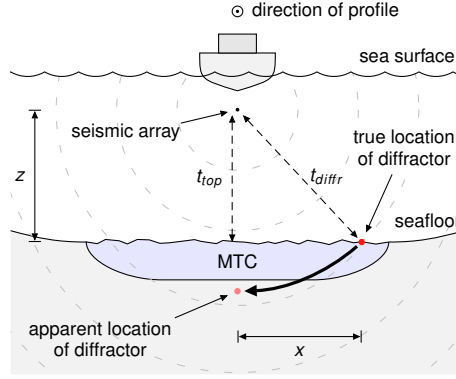


Figure 4. Conceptual diagram oriented perpendicular to a 2-D seismic profile showing how an out-of-plane diffractor at the seafloor will appear to “swing” into the plane of the profile. The seismic source and receiver arrays (seismic datum) and the expanding seismic wavefront are marked. x and z are the the horizontal offset and depth of the diffractor with respect to the seismic array. t_{top} and t_{diff} are the respective two-way travel times to the top of the MTC and to the diffractor.

342 If these assumptions are satisfied, the diffraction shadow provides an estimate of the half-
 343 width of the zone containing the diffractors that swing into the profile. In other words,
 344 it places a lower bound on the width of an MTC from a single 2-D seismic profile.

345 **3.4.1 Controlled Synthetic Demonstration**

346 The aim of this synthetic test is to demonstrate that 3-D information generated
 347 by a heterogeneous geobody is encoded in 2-D seismic profiles by out-of-plane diffrac-
 348 tions, producing a diffraction shadow. If the assumptions above are satisfied, the appar-
 349 ent TWTT to the base of the diffraction shadow can be related to the overall width of
 350 the geobody by Eq. 1.

351 The 3-D synthetic model has dimensions 500 m x 500 m x 500 m with a grid spac-
 352 ing of 1 m. The P-wave velocity is constant, $v_p = 1500 \text{ m s}^{-1}$. The background density
 353 is constant, $\rho = 1400 \text{ kg m}^{-3}$, everywhere except for a half-ellipsoidal region, represent-
 354 ing an MTC, in the centre of the model. Inside the half-ellipsoid zone are randomly lo-
 355 cated $n = 2117$ point diffractors (single cells of higher density, $\rho = 3000 \text{ kg m}^{-3}$). The
 356 3-D, zero-offset seismic response is modelled using one-way wave extrapolation with an
 357 extended split-step scheme (Gazdag & Sguazzero, 1984; Kessinger, 1992) and a 50 Hz

358 Ricker wavelet source signature. The modelled seismic volume, 3-D migration and 2-D
 359 migration of a section through the diffractor zone are presented in Section 4.4.1.

360 **3.4.2 Real Data Demonstration**

361 The aim of this real data test is to demonstrate a practical workflow to assess the
 362 zone of out-of-plane diffractors that contribute to example seismic profile INS2-Line1.
 363 As MTC A is close to the seafloor we can make the simplifying assumption that poten-
 364 tial internal diffractors are at, or near, the seafloor (Section 3.3). This implies $v_{rms} \approx$
 365 $v_{water} = 1500 \text{ m s}^{-1}$. We also assume that the seafloor is equivalent to the potential top
 366 surface of the MTC. The seafloor depth is known independently from multi-beam swath
 367 bathymetry.

368 The workflow to calculate the zone of diffractors that contribute to the image is
 369 as follows:

- 370 1. Pick the apparent base of the diffraction shadow associated with the MTC, t_{diffr} ,
 371 from the diffraction image.
- 372 2. For each interpreted CMP location:
 - 373 (a) Compute the horizontal distance, x , from the CMP to each point on the seafloor.
 - 374 (b) For each point on the seafloor, compute the TWTT from the CMP to the po-
 375 tential top surface of the body, t_{top} , using Eq. 1 with $v_{rms} = 1500 \text{ m s}^{-1}$ and
 376 z equal to the depth of the seafloor.
 - 377 (c) Grid points with TWTT less than the interpreted base diffraction shadow ($t_{top} <$
 378 t_{diffr}) are considered as potential locations for diffractors.

379 **4 Results**

380 **4.1 Diffraction Imaging**

381 **4.1.1 Profile INS2-Line1**

382 The full-wavefield seismic image of the INS2-Line1 profile largely consists of par-
 383 allel, high amplitude Plio-Quaternary reflectors, pierced by the Lolita salt diapir, form-
 384 ing a dome at the seafloor approximately 4 km wide in the centre of the profile (Fig. 5).
 385 The doming has resulted in slope failures that radiate from the centre of the dome, vis-
 386 ible in the bathymetry (Fig. 2b). To the north, the upper Late Quaternary sediments

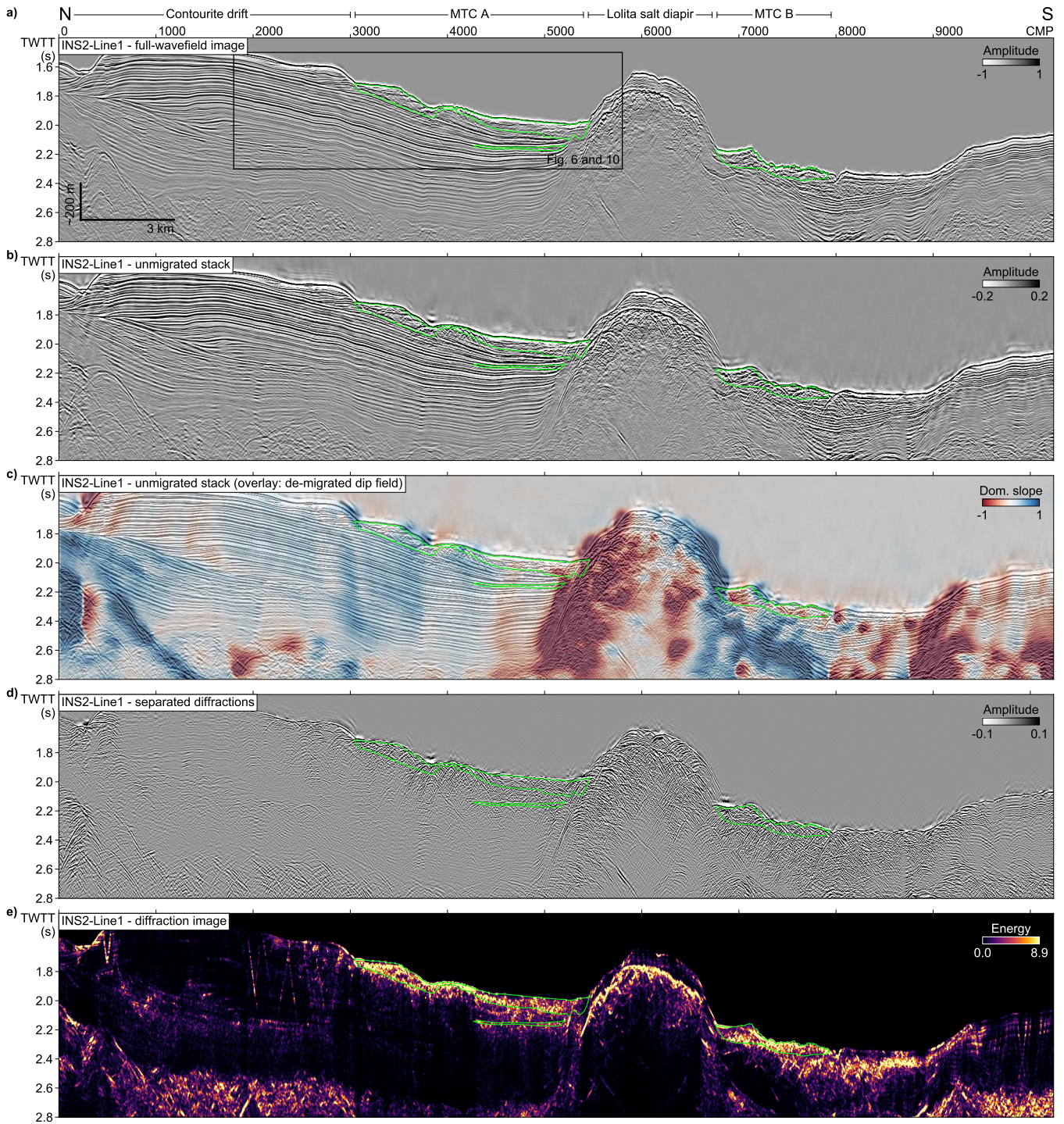


Figure 5. Seismic profile INS2-Line1 from the Portimão Bank area (Fig. 2), MTCs outlined in green. a) Full-wavefield migrated seismic image. b) Unmigrated stacked conventional data (reflections and diffractions). c) De-migrated estimated dip field (dominant slope of reflectors) overlaid on the unmigrated conventional stack. d) Unmigrated stacked separated diffractions. e) Diffraction image.

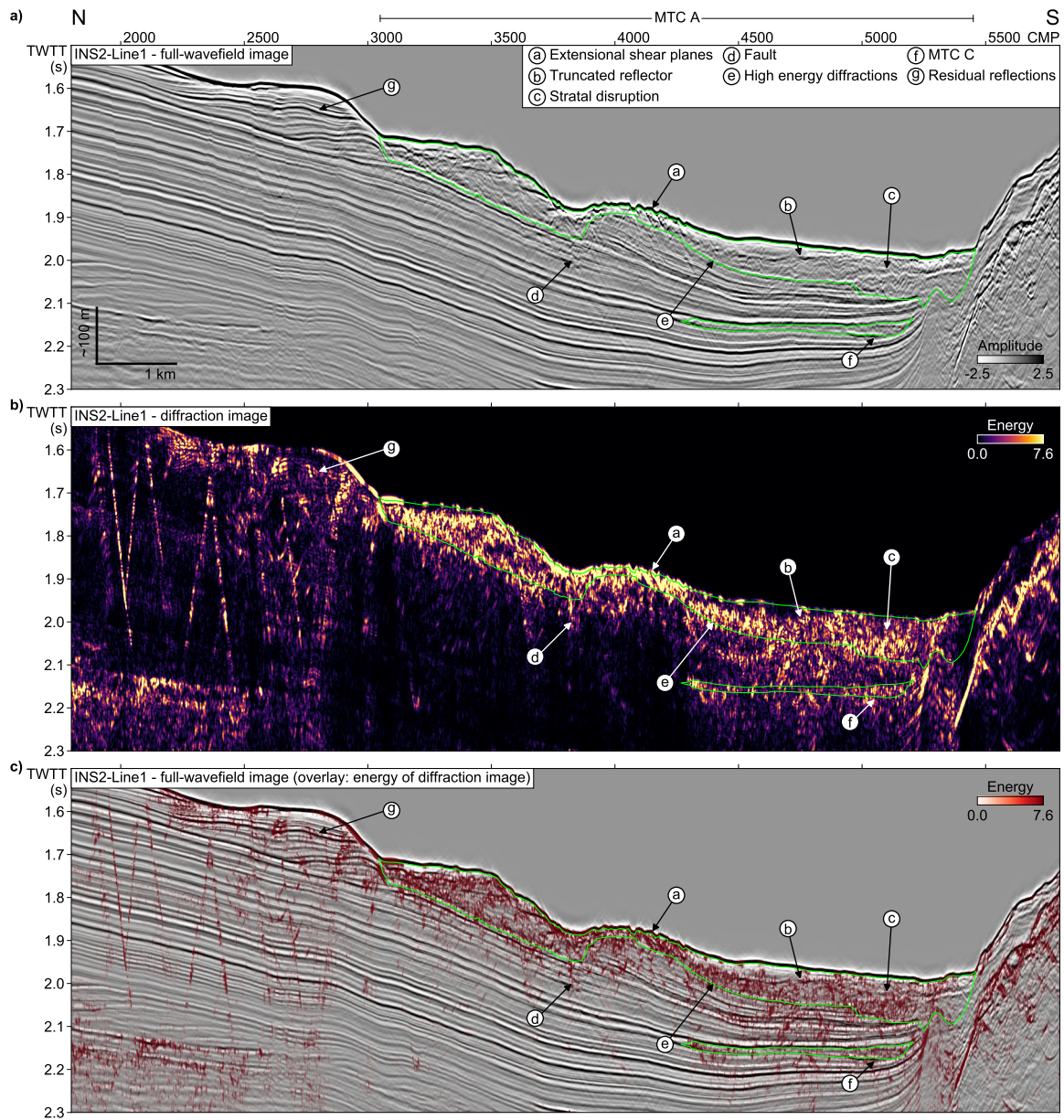


Figure 6. A section of seismic profile INS2-Line1 (Fig. 5) from the Portimão Bank area containing a prominent MTC. Speculative interpreted structure is labelled. a) Full-wavefield seismic image, migrated reflections and diffractions. b) Diffraction image, migrated diffractions. c) Energy of diffraction image overlaid onto full-wavefield image, to highlight location of diffractors.

387 onlap and pinchout, which characterises a major contourite drift deposit resulting from
 388 bottom currents associated with the Mediterranean Outflow Water. Two prominent MTCs
 389 (MTC A and MTC B) are exposed at the seafloor on either side of the diapir and are
 390 clearly visible on the full-wavefield seismic image (Fig. 5a). MTC A has an in-profile length
 391 of approximately 7.4 km and a maximum in-profile thickness of approximately 95 ms TWTT.
 392 MTC B has an in-profile length of approximately 3.7 km and a maximum in-profile thick-
 393 ness of approximately 130 ms TWTT. MTC A originated from the drift deposits, whereas
 394 MTC B originated from the salt diapir. Both propagated towards the south.

395 Fig. 5b shows the unmigrated full-wavefield stack of INS2-Line1. Diffraction tails
 396 are visible originating from the rugose, high amplitude seafloor and top salt interfaces.
 397 Fig. 5c shows the estimated dominant slope of the unmigrated reflectors (de-migrated
 398 dip field estimated from the full-wavefield seismic image) overlaid on the unmigrated stack.
 399 The dip estimate appears to follow the dip of the prominent horizons well.

400 Fig. 5d shows a stack of the separated diffractions. This view is comparable to the
 401 unmigrated stack (Fig. 5b). Diffraction tails are clearly seen throughout the section, in-
 402 cluding from i) a series of normal faults (CMPs 1500 to 3000); ii) inside both prominent
 403 MTCs (CMPs 3000 to 5500 and 7000 to 9000) and iii) within the deeper, chaotic unit
 404 (CMPs 1000 to 5000 and 9000 to 10 000, below around 2.4 s). The diffraction image shows
 405 high amplitudes inside MTC A and MTC B, inside the smaller MTC C (below MTC A),
 406 at the rugose top salt interface and within the deeper chaotic unit (Fig. 5e). Some resid-
 407 ual reflection energy remains, particularly in areas of rapidly varying dip (see Fig. 6, la-
 408 bel “g”).

409 **4.1.2 Profile MP06b**

410 The MP06b seismic profile is a cross-sectional view of the Marquês de Pombal fault
 411 (Fig. 7 and Fig. 8e). The profile can be divided into two main sections: the Infante Don
 412 Henrique Basin (the footwall of the Marquês de Pombal fault) and the steeply dipping
 413 slope area (the frontal part of the hanging wall of the fault). The full-wavefield seismic
 414 image (Fig. 7a and Fig. 8a) shows that the Infante Don Henrique Basin contains a >1 s
 415 TWTT thick, stacked succession of MTCs with apparently chaotic to transparent seis-
 416 mic character, separated by parallel horizons representing the unfailed confining sedi-
 417 ments. The hanging wall of the Marquês de Pombal fault shows greater deformation—

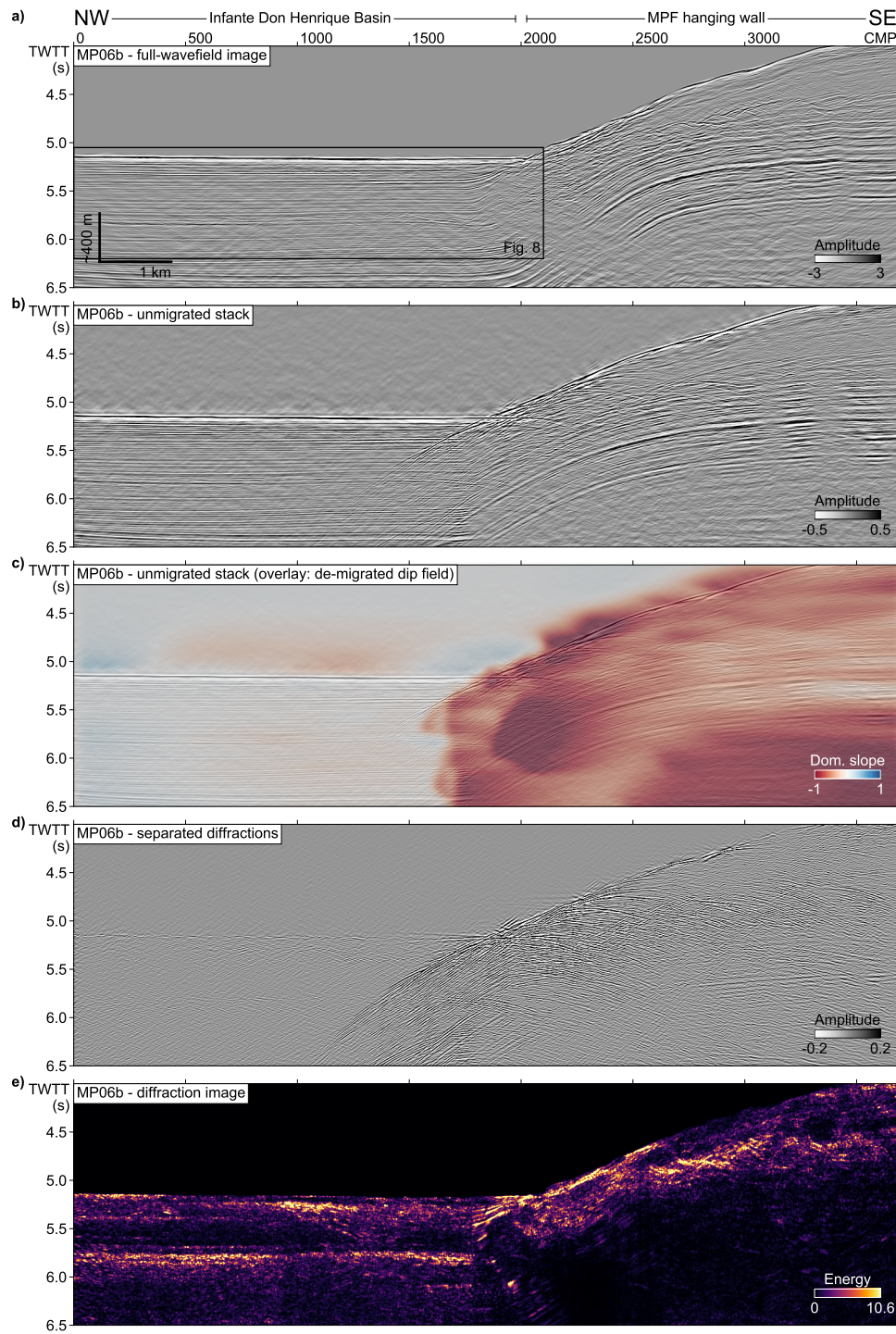


Figure 7. Seismic profile MP06b from the Marquês de Pombal fault zone area (Fig. 2). The Marquês de Pombal fault (MPF) is located around CMP 2000. a) Full-wavefield migrated seismic image. b) Unmigrated stacked full-wavefield data. c) De-migrated estimated dip field (dominant slope of reflectors) overlaid on the unmigrated full-wavefield stack. d) Unmigrated stacked separated diffractions. e) Diffraction image.

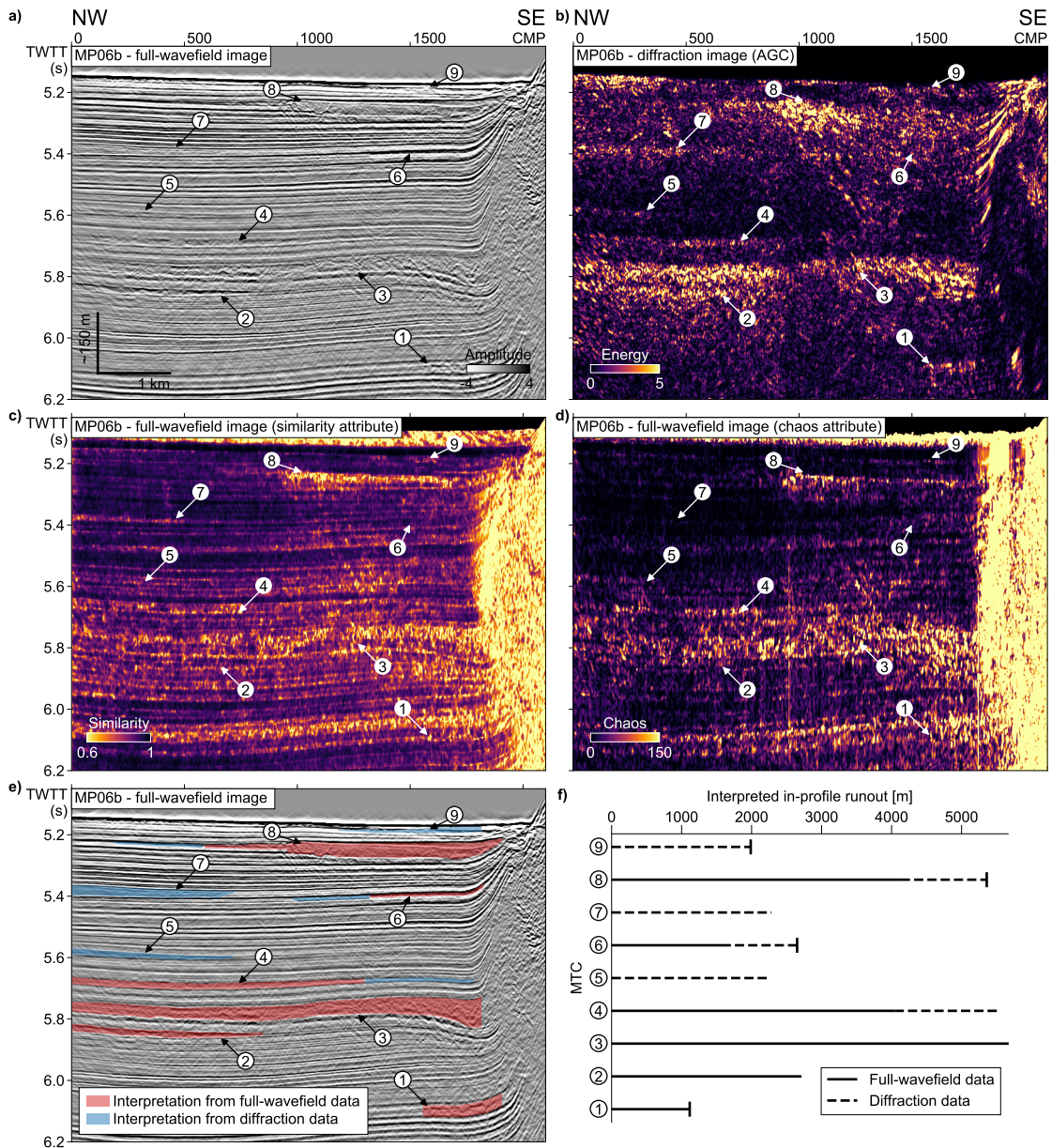


Figure 8. A section of seismic profile MP06b from the Marquês de Pombal fault area (Fig. 7). Interpreted MTCs are labelled from 1 to 9. a) Conventional full-wavefield seismic image. b) Diffraction image. c) The similarity attribute and d) the chaos attribute derived from the full-wavefield seismic image. e) The interpreted MTCs overlaid on the full-wavefield image. The extent of the bodies interpretable from the full-wavefield images and attributes is shaded red, the (extra) extent interpretable from the diffraction image is shaded blue. f) The proportion of the apparent in-profile runout length of each body interpreted from the full-wavefield image and attributes compared to that interpreted from the diffraction image.

418 the shallow part of the slope shows extremely disordered, overlapping horizons that re-
 419 flect the complex seafloor topography caused by mass-wasting in the slope area. The Marquês
 420 de Pombal fault plane is not directly imaged in this data; the fault zone is represented
 421 by a zone of relatively low amplitude, disordered reflectors, dipping to the south east (CMPs
 422 1900 to 2500, 5.25 s to 6.5 s TWTT).

423 Fig. 7b shows the unmigrated stack of MP06b. Diffraction tails are visible origi-
 424 nating from the rugose seafloor in the steeply dipping hanging wall area (CDPs 1800 to
 425 3000) and from truncated reflectors where the Infante Don Henrique Basin meets the low
 426 amplitude, disordered zone containing the Marquês de Pombal fault. Fig. 7c shows the
 427 estimated dominant slope (de-migrated dip field estimated from Fig. 7a) overlaid on the
 428 unmigrated stack. In general, the dominant slope appears to follow the dip of the promi-
 429 nent horizons well, showing near-zero slope in the Infante Don Henrique Basin and neg-
 430 ative slope (dipping to the north west) in the hanging wall area. The south eastern, deep
 431 corner of the profile (CMPs >2500, >5.5 s TWTT) shows anomalously high slope val-
 432 ues, corresponding to steeply dipping noise, due to low signal-to-noise ratio in this deeper
 433 area. Fig. 7d shows a stack of the separated diffractions. This section is comparable to
 434 the unmigrated stack (Fig. 7b). Diffraction tails are clearly seen throughout the section,
 435 particularly from disrupted reflectors in the hanging wall area (CMPs 2000 to 4200) and
 436 corresponding to MTCs in the Infante Don Henrique Basin (CMPs 0 to 2000, 5.2–6 s TWTT).
 437 Fig. 7e shows the diffraction image (i.e., the separated diffractions after migration). The
 438 diffraction image shows laterally continuous, high amplitude zones that correspond to
 439 MTCs seen in the full-wavefield seismic image. Some residual reflection energy remains,
 440 particularly in the area of rapidly varying dip at the break in slope corresponding to the
 441 Marquês de Pombal fault (CDP 2000).

442 **4.2 Comparison of Full-Wavefield and Diffraction Images of Internal Stru-** 443 **ture**

444 Fig. 6 shows a section of seismic profile INS2-Line1 around MTC A, exposed at the
 445 seafloor (Fig. 5). It shows the full-wavefield seismic image (Fig. 6a), the corresponding
 446 diffraction image (Fig. 6b) and the diffraction image overlaid on the full-wavefield im-
 447 age (Fig. 6c). Diffraction energy is concentrated inside MTC A compared to the unfailed
 448 underlying sediments. We speculate that these high amplitude diffractions could result
 449 from: (a) faults or shear planes in an extensional part of the MTC; (b) a truncated in-

450 ternal reflector within the MTC; (c) a zone of intense stratal disruption within the MTC
 451 (possibly the interface between two separate mass-transport deposits); (d) a small nor-
 452 mal fault directly beneath the MTC, likely related to sediment loading/unloading after
 453 failure; (e) a zone of diffuse, high energy diffractions that is not clearly related to struc-
 454 ture resolved by the reflection image and (f) a smaller, deeper MTC (MTC C). The re-
 455 maining diffraction energy within the MTC has complex geometry and is not clearly re-
 456 lated to structure resolved by the reflection image (e.g., the area labelled “e”).

457 **4.3 Comparison of Diffraction Image with Discontinuity Attributes**

458 Fig. 8 shows a section of seismic profile MP06b, focused on the stacked succession
 459 of MTCs in the Infante Don Henrique Basin. Fig. 8a shows the full-wavefield seismic im-
 460 age, Fig. 8c shows the similarity attribute of the full-wavefield image (similarity attribute
 461 implementation from OpendTect 6.4 with a time gate of 10 ms) and Fig. 8d shows the
 462 chaos attribute of the full-wavefield image (“Chaotic Reflection” attribute implementa-
 463 tion from Kingdom Rock Solid Attributes). Fig. 8b shows the corresponding diffraction
 464 image.

465 Interpretation of the MTCs is guided by one or more of the following features: i)
 466 apparently chaotic or transparent seismic character in the full-wavefield seismic image;
 467 ii) high amplitude, laterally continuous top and/or basal bounding reflections; iii) lobe
 468 shaped, laterally consistent low similarity/high chaos values or iv) lobe shaped, later-
 469 ally consistent high amplitude diffraction energy. In total, nine MTCs are interpreted
 470 from a combination of the full-wavefield image, derived attributes and the diffraction im-
 471 age (labelled in order of decreasing depth from MTC1 to MTC9). Three large bodies are
 472 directly visible in the full-wavefield seismic image (MTC3, MTC4 and MTC8). Two other
 473 bodies are clearly resolved only by the diffraction image (MTC5 and MTC7).

474 Fig. 8e shows the interpreted lateral extent and thickness of the interpreted bod-
 475 ies overlaid on the full-wavefield seismic image. The portion of the bodies interpreted
 476 from the full-wavefield image and attributes versus the diffraction image is indicated. Fig. 8f
 477 shows the interpreted length (apparent in-profile runout) of these bodies, indicating the
 478 proportion of the total length interpretable only from the diffraction products. Several
 479 of the bodies (MTC2, MTC3, MTC4, MTC5 and MTC7) extend past the end of the sec-
 480 tion, in these cases the interpreted runout length is a lower bound on their total runout

481 length in the direction of the profile. MTC4 and MTC6 are both resolved from the full-
 482 wavefield products, but by using the diffraction image their in-profile runout length is
 483 extended by >1.5 km and 1.1 km respectively. MTC7 is only clearly resolved by the diffrac-
 484 tion image, likely because it has an apparently transparent seismic character in the full-
 485 wavefield seismic image, whereas the diffraction image clearly resolves a lobe shaped zone
 486 of heterogeneity. MTC9 is a 2 km long body near the seafloor that is only visible in the
 487 diffraction image, likely because it is thin enough to be masked in the full-wavefield seis-
 488 mic image by the high amplitude, long wavelength seismic reflections.

489 **4.4 Constraining the Location of Out-of-Plane Diffractors**

490 ***4.4.1 Controlled Synthetic Demonstration***

491 Fig. 9 shows the results of the controlled synthetic demonstration of the “diffrac-
 492 tion shadow” concept. This demonstration models an MTC body as a half-ellipsoid con-
 493 taining randomly placed point diffractors. Fig. 9a shows the top and base boundaries
 494 of the body and the point diffractors (single cell density anomalies). Fig. 9b shows the
 495 forward modelled zero-offset volume in time domain. As the model is composed entirely
 496 of diffractors (no reflections), this is equivalent to the separated diffracted wavefield. Fig. 9c
 497 shows the zero-offset volume after migration with a 3-D constant velocity ($v_p = 1500 \text{ m s}^{-1}$)
 498 Stolt migration (Stolt, 1978). The diffractions are properly focused back to their apexes,
 499 which lie within the boundaries of the body (converted to TWTT). Some energy lies slightly
 500 outside these boundaries, due to the band-limited, zero-phase source wavelet. Fig. 9d
 501 shows a single 2-D section of the volume at $y = 250 \text{ m}$, migrated with an equivalent 2-
 502 D constant velocity Stolt migration. Out-of-plane diffracted energy is not properly im-
 503 aged by the 2-D migration. The result is a generally chaotic internal seismic character
 504 within the body (compare to Fig. 9c) and a diffraction shadow that extends up to ap-
 505 proximately 20 ms beneath the base of the body. The extent of the diffraction shadow
 506 agrees well with the predicted maximum extent based on the width of the body and Eq. 1.

507 ***4.4.2 Real data application***

508 Figs. 10a and 10b show the true basal surface of MTC A picked from the full-wavefield
 509 seismic image (INS2-Line1), alongside the picked base of the diffraction shadow, the limit
 510 of diffractions interpreted to be associated with MTC A. Fig. 10c shows the lateral ex-

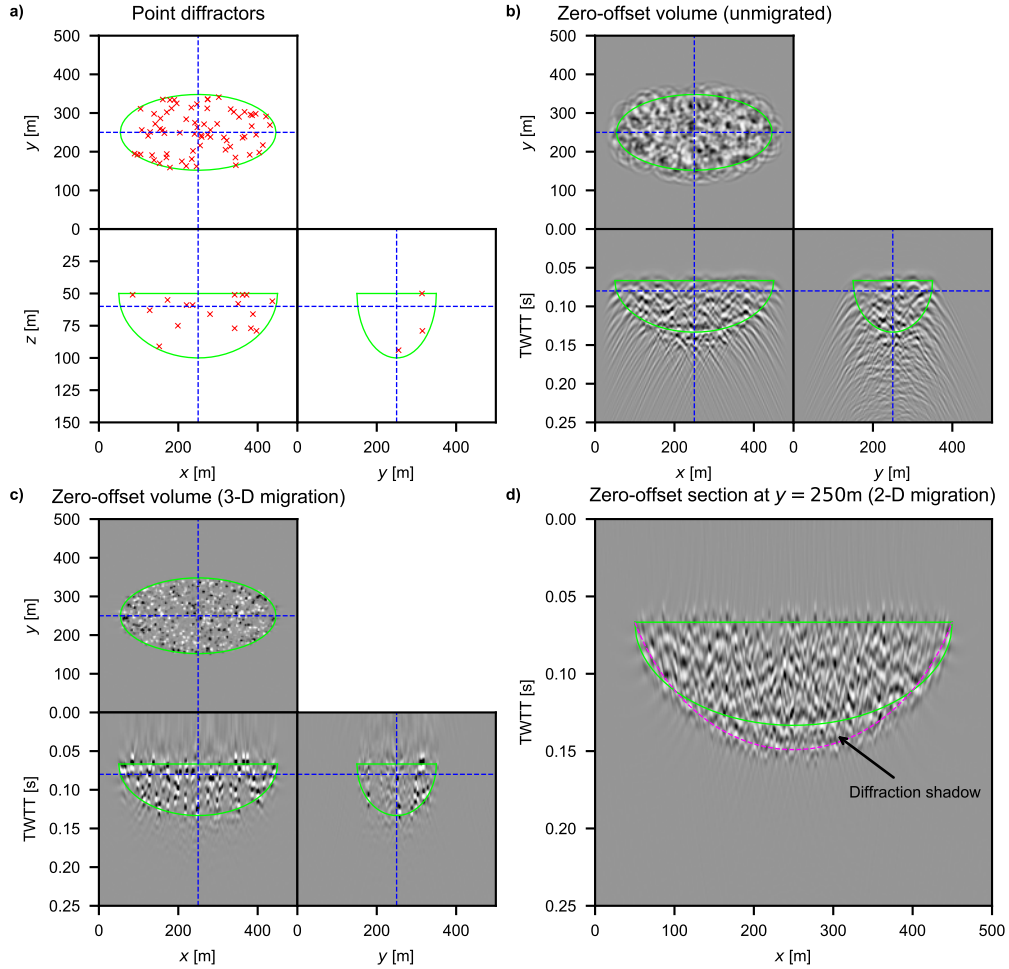


Figure 9. Controlled synthetic demonstration model setup and results. The boundaries of the half-ellipsoidal zone representing an MTC are outlined in green. a) 3-D model definition showing location of point diffractors (single-cell density anomalies) randomly placed within the MTC zone. b) 3-D forward modelled zero-offset volume. c) 3-D Stolt migration of (b). d) 2-D Stolt migration of a 2-D slice of (b) at $y = 250$. The base of the diffraction shadow predicted by Eq. 1 is shown in dashed magenta.

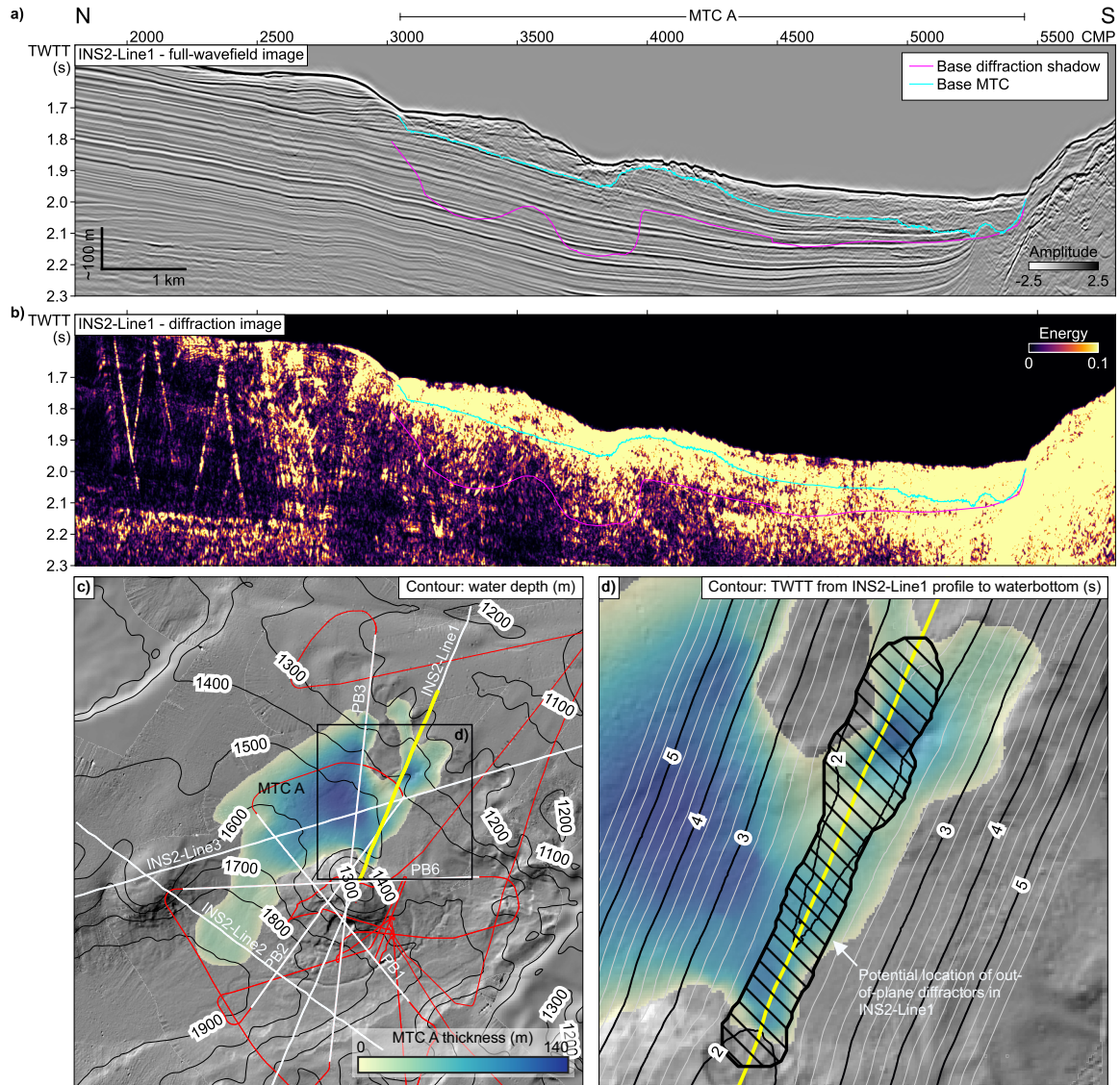


Figure 10. A section of seismic profile INS2-Line1 (Fig. 5) containing MTC A. a) The full-wavefield seismic image. b) The corresponding diffraction image. The blue horizon is the interpreted basal surface from the full-wavefield image, the pink horizon is the interpreted base of the out-of-plane diffractions associated with MTC A (the diffraction shadow). c) Water depth (contours) on the shaded relief of the area surrounding the Lolita salt diapir. The extent and thickness of MTC A is interpreted from the bathymetry, sub-bottom profiler data (red) and a network of multi-channel seismic profiles (white). d) The two-way travel time (TWTT) contour from INS2-Line profile seismic datum to the potential top MTC A surface (seafloor) (maximum record length is 5.8 s). The hatched black area indicates the zone of potential locations for the out-of-plane diffractors.

511 tent and thickness of MTC A, interpreted from a combination of multi-channel seismic
 512 and sub-bottom profiler lines and the bathymetry, giving a total volume of 5.5 km^3 (con-
 513 verted from time to depth using the sediment velocity gradient of 200 ms^{-2}). The method-
 514 ology, multi-channel seismic profiles and an example of one of the sub-bottom profiles
 515 are presented in the supplementary information (Text S2 and Figs. S1-S4). Fig. 10d shows
 516 the TWTT contour to the potential top surface of MTC A (the seafloor) from seismic
 517 profile INS2-Line1 (calculated using Eq. 1), with the TWTT of the base diffraction shadow
 518 overlaid (black hatched area). This area shows the zone, perpendicular to the profile, of
 519 the potential locations of diffractors that could contribute to the diffraction shadow as-
 520 sociated with MTC A. The half-width varies from a minimum of 422 m to a maximum
 521 of 886 m, implying that diffraction energy from at least 886 m from the vertical plane of
 522 the profile has contributed to the image.

523 **5 Discussion**

524 **5.1 Imaging Internal Structure**

525 The diffraction image for profile INS2-Line1 (Fig. 6) clearly shows a zone of nor-
 526 mal faults between CMPs 1800 to 3000 and the rugose top salt interface of the Lolita
 527 salt diapir—both classic targets for diffraction imaging. The zone of normal faults ap-
 528 pears significantly more well-defined in comparison to the full-wavefield image. There
 529 is also a significantly higher concentration of diffraction energy within MTC A compared
 530 to the surrounding unfailed sediments. This suggests that the internal structure of MTC
 531 A contains significantly more wavelength and sub-wavelength scale discontinuities com-
 532 pared to the unfailed sediments, which can already be seen from the full-wavefield seis-
 533 mic image. This is consistent with outcrop examples of MTCs, which show that com-
 534 plex internal structure can be preserved (Lucente & Pini, 2003). We observe high am-
 535 plitude diffractors that coincide with structure observed on the reflection image related
 536 to MTC A: headscarp faults, truncated internal interfaces and strong stratal disruption.
 537 This is the type of small-scale (i.e., potentially sub-wavelength) geological heterogene-
 538 ity that we would expect to generate diffractions (Fig. 1).

539 Diffractors that do not coincide with structure seen in the full-wavefield seismic im-
 540 age are also resolved (labelled “e” in Fig. 6). In the absence of high-resolution data, such
 541 as cores or sub-bottom profiler images, it is not clear exactly what structure this rep-

542 represents, but we speculate that these may be related to small-scale internal structure that
543 is not well imaged by the full-wavefield image, such as local shear zones, intact embed-
544 ded blocks or fluid escape features. Diffractions require both lateral heterogeneity (around
545 or below the scale of the seismic wavelength) *and* an impedance contrast, so the pres-
546 ence of diffractions within a body is evidence that significant wavelength-scale (i.e, me-
547 tre to decametre) internal structure is preserved after transport or generated during em-
548 placement. Diffraction images can thus provide information on the degree of internal dis-
549 aggregation or organisation by quantifying the degree of geological heterogeneity at scales
550 close to the seismic resolution. High diffraction energy within an MTC is likely to be as-
551 sociated with relatively low disaggregation, as it implies that wavelength-scale internal
552 structure is preserved. Conversely, low diffraction energy within an MTC could imply
553 significant disaggregation—the scale of internal structure has been reduced to much lower
554 than the seismic wavelength by mass-movement processes. The magnitude of the diffrac-
555 tion energy could therefore provide an extra source of information to constrain flow type,
556 for example to differentiate between debris flows (complete disaggregation and destruc-
557 tion of pre-failure internal interfaces), slumps (pre-failure internal interfaces deformed
558 but largely preserved) and the transition between both end members. The high ampli-
559 tude diffraction image response observed in Fig. 6b supports an interpretation of MTC
560 A as a “structured” rather than “structureless” deposit, even if the geometry of such struc-
561 ture is not well-resolved by the seismic profiles used in this study.

562 We also clearly resolve a normal fault plane *below* MTC A in the diffraction im-
563 age (labelled “d” in Fig. 6). This is associated with an approximately 500 m wide, channel-
564 shaped depression on the top surface of MTC A around CMP 3750. We interpret this
565 to be the result of sediment loading due to the emplacement of MTC A on the previ-
566 ously competent sediments, as the fault becomes blind at depth. As well as resolving struc-
567 ture within MTCs, diffraction imaging is able to image small-scale, discontinuous struc-
568 ture in the unfailed sediments immediately *below* the basal shear surface.

569 **5.2 Discrimination of Events Near the Limit of Seismic Resolution**

570 The Infante Don Henrique basin hosts a >1 s TWTT thick succession of stacked
571 MTCs (Fig. 8). Some large events in profile MP06b ($n = 6$) are clearly visible on the
572 full-wavefield seismic image as apparently chaotic bodies with well-defined top and basal
573 reflectors. The diffraction image, however, reveals several smaller events ($n = 3$) that

574 are difficult to identify or are ambiguous in the full-wavefield seismic image and associ-
575 ated discontinuity attributes. In addition, the diffraction image allows better definition
576 of the apparent lateral extent (runout) of bodies. We are able to follow the apparent in-
577 profile runout of some events for significant extra distance (on the order of kilometres
578 for seismic profile MP06b) compared to the full-wavefield seismic image (Fig. 8f).

579 We also observe this effect on seismic profile INS2-Line1 (Fig. 6). Here, there is a
580 small MTC (MTC C, labelled “f” in Fig. 6) below the larger event, MTC A. In the full-
581 wavefield seismic image MTC C is represented by a short (less than 500 m), high am-
582 plitude basal horizon. The diffraction image clearly shows a lobe shaped zone of hetero-
583 geneity, approximately 500 m in length, that we interpret as a small MTC that failed to-
584 wards the north, originating from the dome associated with the Lolita salt diapir.

585 Diffraction images in general offer higher lateral (i.e., horizontal) resolution because
586 they overcome the lateral resolution limit of seismic reflections. In the context of screen-
587 ing for MTCs, diffraction images also clearly improve the discrimination of relatively small,
588 thin events (on the order of 10 ms TWTT thick, Fig. 8). This improvement is a result
589 of removing the relatively high amplitude reflections, which can mask thin zones of dis-
590 continuous geology. In the MP06b profile, the unfailed confining sediments have a seis-
591 mic character dominated by high amplitude, long wavelength reflections that are par-
592 allel to the MTCs. In addition, the MTCs themselves generate strong reflections at their
593 top and basal surfaces. The apparent vertical thickness of these reflections is related to
594 the dominant wavelength of the seismic source and is independent of the thickness of the
595 body. This means that the relatively high amplitude and long wavelength reflections can
596 mask thin, discontinuous geobodies that may otherwise be properly imaged by full-wavefield
597 seismic imaging. By eliminating these masking reflections, the effective *interpretable* ver-
598 tical resolution is increased for discontinuous, diffraction generating bodies that are thin-
599 ner than the dominant seismic wavelength.

600 Consequently, diffraction images allow more accurate delineation of the total lat-
601 eral extent of MTCs when a significant proportion of the body is thinner than the re-
602 flection image can resolve. This is particularly important to characterise the flow prop-
603 erties of unconfined mass-movements from seismic data. Many events have a substan-
604 tial component of fine sediment that runs out a significant distance beyond the main co-
605 hesive body of the event, pinching out at zero thickness at the true maximum extent of

606 the flow. This type of thin deposit, parallel to the background sedimentation, is difficult
607 to image with full-wavefield seismic images for the reasons outlined above.

608 The record of buried MTCs identified from marine geophysical data is biased to-
609 ward events that can be clearly resolved in multi-channel seismic reflection images (i.e.,
610 relatively thick and laterally extensive). This means that catalogues of MTCs are biased
611 towards larger events, or younger events that are still preserved in the bathymetry (Urgeles
612 & Camerlenghi, 2013). Screening for MTCs using diffraction imaging will allow for a more
613 complete catalogue of smaller, deeper events, with more confident delineation of their
614 true total runout.

615 **5.3 Comparison to Seismic Discontinuity Attributes**

616 Seismic discontinuity attributes are routinely computed as part of a traditional geo-
617 hazard interpretation workflow in order to screen for, characterise and delineate MTCs
618 (e.g., Alves et al., 2014; Bhatnagar et al., 2019). Here, we calculate the similarity and
619 chaos attributes of the full-wavefield seismic image to compare to the diffraction image
620 (Fig. 8). There are high-level similarities: areas with low similarity and high chaos val-
621 ues tend to correspond to areas of high diffraction energy. Relatively large events (MTC3,
622 MTC4 and MTC8) are clearly imaged by both attributes and by the diffraction image.
623 Several smaller events, however, are not clearly delineated from the background geology
624 by the discontinuity attributes. Moreover, both the chaos and similarity attribute seem
625 to be sensitive to features other than geological discontinuities—we observe low similar-
626 ity, high chaos values for high amplitude, laterally continuous horizons (i.e., reflections)
627 in the unfailed sediments that host the MTCs. It is difficult to discriminate a high am-
628 plitude, horizontal unfailed horizon from a thin MTC using these discontinuity attributes.

629 We argue that when screening for MTCs, diffraction images may be a more “phys-
630 ically correct” alternative to traditional discontinuity attributes of full-wavefield images
631 because:

- 632 1. they are directly sensitive to the target geology (i.e., bodies likely to contain wave-
633 length and sub-wavelength scale discontinuities).
- 634 2. relatively high amplitude, long wavelength coherent reflections—which can inter-
635 fere with attributes and mask thin bodies—are eliminated.

- 636 3. they do not suffer from edge effects and smoothing that may be introduced by window-
637 based attributes.

638 **5.4 Constraining the Lateral Extent of MTCs From 2-D Profiles**

639 Seismic imaging in 2-D assumes that the recorded energy is reflected or diffracted
640 from the 2-D vertical plane along the seismic profile. This may be a reasonable assump-
641 tion where geological structure is 1-D perpendicular to the plane of the profile (a so-called
642 *dip line*). When reflectors dip obliquely with respect to the profile, reflections cannot be
643 properly imaged with a 2-D migration. Energy reflected from out-of-plane is not prop-
644 erly located in TWT and may interfere with primary in-plane energy. MTCs are in-
645 herently 3-D geobodies—in addition to internal structure, they often show rugose, non-
646 conformal upper and basal surfaces and vertical lateral margins that can generate high
647 amplitude reflections and diffractions (Fig. 1). This means that there is rarely an op-
648 timal direction to acquire a well-imaged 2-D seismic “dip line” across an MTC. In other
649 words, out-of-plane energy is a common feature of 2-D seismic images of MTCs. The su-
650 perior illumination of diffractions means that diffraction images will contain proportion-
651 ally more out-of-plane energy than full-wavefield images.

652 Fig. 9 demonstrates this effect with a controlled synthetic test, where an MTC body
653 is simulated as a half-ellipsoidal zone of point diffractors. The results show that while
654 a 3-D migration is properly able to image and locate diffractors in space, a 2-D seismic
655 acquisition and image will inevitably contain a large proportion of out-of-plane diffrac-
656 tions. The 2-D migrated section (Fig. 9d) shows an apparently “chaotic” texture, de-
657 spite there being no chaotic reflectors inside the MTC. We speculate that out-of-plane
658 diffractions could be partly responsible for the infamous apparently chaotic internal seis-
659 mic response of MTCs in 2-D seismic profiles. The result underlines the importance of
660 acquiring 3-D seismic data for good imaging and proper reconstruction of the geome-
661 try of the internal structure of MTCs, for both conventional full-wavefield seismic imag-
662 ing and for diffraction imaging.

663 In Section 3.4 we propose a simple workflow to constrain the original location of
664 out-of-plane diffracted energy imaged in a 2-D seismic profile. Under certain (strong)
665 assumptions the results can be used to estimate a minimum bound on the lateral extent,
666 perpendicular to the profile, of the zone of diffractors that contribute to the diffraction

667 image—a constraint on the minimum half-width of an MTC imaged by a 2-D seismic
668 profile. The controlled synthetic test shows that Eq. 1 can predict the apparent thick-
669 ness of this diffraction shadow (Fig. 9d). We then demonstrate the method on a real data
670 example by applying it to profile INS2-Line1, where there is a clearly visible diffraction
671 shadow beneath MTC A (Fig. 10). The presence of such diffractions beneath the appar-
672 ent basal surface, but clearly associated with MTC A, indicates that the diffraction im-
673 age contains energy from outside the plane of the profile. Does this real data example
674 satisfy the assumptions stated in Section 3.4? It seems reasonable to assume that this
675 MTC does contain diffractors spread throughout the body, as we consistently see an el-
676 evated response in the diffraction image throughout the 2-D profile in a downslope di-
677 rection (Fig. 6). The maximum TWTT thickness of MTC A is approximately 150 ms at
678 a depth of approximately 1.7 s TWTT, therefore we can consider this MTC to be a “thin
679 body”. MTC A is exposed at the seafloor, so we can be confident that the overburden
680 velocity is constant velocity (water velocity) and laterally homogeneous perpendicular
681 to the profile. The remaining assumption is that there exists a clearly defined diffrac-
682 tion shadow associated with the body. In the lower part of the body, the diffraction shadow
683 is clearly associated with MTC A, like in the controlled synthetic test. In the upper part
684 of the body, however, there is significant uncertainty around whether the interpreted diffrac-
685 tors are associated with the MTC. For this real data example, the resulting zone of po-
686 tential diffractors has half-width comparable to or lower than the distance to the edge
687 of MTC A in the direction of maximum extent (Fig. 10d). This indicates that perhaps
688 this zone of potential diffractors could be a realistic lower bound on the width of the MTC
689 with respect to the seismic profile. On the other hand, interpreting the base of the diffrac-
690 tion shadow will always be the part of this workflow that introduces the greatest uncer-
691 tainty. Whilst it is a crude technique, with large errors, it is still an informative exer-
692 cise to think about where these out-of-plane diffractors could come from, and how this
693 relates to the overall geometry of an imaged MTC.

694 The method proposed in Section 3.4 is simple but nevertheless could be a useful
695 way to estimate a lower bound on the extent of MTCs from a single 2-D seismic profile,
696 where other geophysical information is not available. This is a common scenario when
697 screening for MTCs for marine geohazard studies in frontier areas; for academic and vin-
698 tage datasets; and in polar areas, where acquiring 3-D towed-streamer seismic data may
699 be impossible due to year-round ice cover. It is trivial to extend the method to deal with

700 buried MTCs, so long as i) the velocity model to the top of the body is known; ii) the
701 slide is thin relative to its depth; and iii) the topography of the top surface is small, rel-
702 ative to its depth. Future studies should validate this approach for a realistic scenario
703 by repeating the workflow for the controlled synthetic test with a 2-D profile extracted
704 from a real data 3-D volume.

705 **5.5 Limitations of Diffraction Imaging to Characterise MTCs**

706 Whilst we have shown that diffraction images clearly offer better imaging of small-
707 scale discontinuous geology compared to reflection images, there remain some limitations,
708 particularly regarding the data used for this study and the specific application to char-
709 acterise MTCs.

710 **5.5.1 Incomplete Diffraction Separation**

711 Diffraction imaging relies on good separation between the diffracted and reflected
712 wavefields. Here, we perform the diffraction separation in common-offset domain using
713 PWD filters to eliminate laterally continuous reflections. Subaqueous mass-failures tend
714 to occur in environments that are geologically complex, such as canyons, tectonically ac-
715 tive areas and diapiric areas. This means that seismic images in such environments are
716 also likely to contain strong variation in dip, reflections that are not laterally continu-
717 ous and high amplitude reflections and diffraction tails generated by a rugose seafloor.
718 These factors can prevent reliable estimation of the true dip field from unmigrated seis-
719 mic profiles. Our solution is to estimate the dip field on migrated data, and de-migrate
720 the dip field for diffraction separation on the unmigrated common-offset sections. In gen-
721 eral, the results of the dip estimation and de-migration are adequate for diffraction sep-
722 aration to image the shallow MTCs in this study. There are, however, some residual re-
723 flections that are not eliminated during diffraction separation, contaminating the diffrac-
724 tion images (Section 4.1). Fortunately, residual reflections are straightforward to iden-
725 tify in the diffraction image, because they appear at the same location as in the full-wavefield
726 image.

727 Other diffraction separation methods may be better suited to imaging MTCs in
728 geologically complex settings. These include post-migration diffraction separation in dip-
729 angle domain (Reshef & Landa, 2009) and diffraction separation by adaptive subtrac-

730 tion of the coherent reflected wavefield (Schwarz, 2019a). The choice of method ultimately
731 depends on the seismic acquisition (e.g., streamer length compared to target depth, lat-
732 eral and vertical image resolution, 2-D vs 3-D acquisition geometry), data characteris-
733 tics (e.g., amplitude of diffractions relative to reflections, noise level) and confidence in
734 the velocity model. In all cases, the pre-processing flow must be designed to preserve diffrac-
735 tion energy.

736 *5.5.2 Migration Velocities*

737 For the seismic profiles analysed in this study, migration velocity analysis by fo-
738 cusing diffractions or moveout analysis of reflections was not possible (Section 3.3). The
739 data were acquired using a short streamer relative to the water depth, so there is no sig-
740 nificant differential moveout of reflection events in common-midpoint domain to perform
741 a robust semblance-based velocity analysis. We found that the separated diffracted wave-
742 field was routinely contaminated with out-of-plane diffractions, which would focus diffrac-
743 tions at an incorrect velocity and at an incorrect TWTT. Instead, we used migration ve-
744 locities derived from simple velocity gradients in the shallow sediments, as our target MTCs
745 are shallow with respect to the water depth. A test of the sensitivity of diffraction imag-
746 ing to the chosen migration velocity is presented in the supplementary information (Fig. S7).

747 Future studies should concentrate on mitigating the effect of out-of-plane diffrac-
748 tions for focusing migration velocity analysis from 2-D seismic profiles. This could be
749 achieved by weighting the focusing analysis towards continuous diffraction generating
750 structures such as faults, or deeper diffractors that are less biased by not being exactly
751 in-plane. The problem of out-of-plane diffractions is resolved with 3-D seismic data, be-
752 cause 3-D migrations can collapse diffractions to their true apex.

753 **6 Conclusions**

754 We use two 2-D marine multi-channel seismic profiles from the Gulf of Cadiz, south
755 west Iberian Margin to compare the ability of seismic diffraction imaging to conventional
756 full-wavefield seismic imaging to characterise MTCs. We find that in these examples MTCs
757 generate a relatively large contribution of diffracted energy compared to the surround-
758 ing unfailed confining sediments, likely because the scale of their internal structure and
759 rugose erosional basal surface is close to or below the scale of the seismic wavelength.

760 Diffraction images can be considered to primarily image small-scale, discontinuous ge-
 761 ological structure and have higher lateral resolution in comparison to full-wavefield seis-
 762 mic images. By overlaying the diffraction images on the full-wavefield seismic images we
 763 show that the diffraction images can resolve internal structure within such bodies. We
 764 speculate that the remaining diffraction energy is related to small-scale structure that
 765 is below the resolution of the reflection image.

766 Our results suggest that diffraction imaging can be:

- 767 1. used to quantify the degree of heterogeneity within a body, important for assess-
 768 ing the degree of disaggregation from transport and emplacement.
- 769 2. considered as a more physically justified alternative to traditional seismic discon-
 770 tinuity attributes, because it directly images subsurface heterogeneity.
- 771 3. an alternative to seismic discontinuity attributes to better delineate relatively small
 772 or thin bodies that are close to the resolution of the full-wavefield seismic image.
- 773 4. used to estimate a minimum bound on the half-width perpendicular to a 2-D seis-
 774 mic profile of MTCs, under certain conditions and strong assumptions.

775 Characterisation of MTCs and their internal structure is a promising new appli-
 776 cation of diffraction imaging, potentially bridging the “resolution gap” between seismic
 777 data and outcrop studies. Our results underline the importance of preserving diffractions
 778 through the processing flow for lateral resolution (including for full-wavefield seismic im-
 779 ages), and the importance of 3-D seismic imaging to characterise complex geology such
 780 as MTCs.

781 **Appendix A Dip De-migration**

782 The aim of dip de-migration is to recover the unmigrated dip field from a dip field
 783 estimated on a migrated image. We use this technique due to the presence of high am-
 784 plitude, steeply dipping diffraction tails and poor reflector continuity throughout the un-
 785 migrated data used in this study.

786 We perform the dip de-migration using simple geometric relations that describe how
 787 migration affects dipping reflectors in 2-D (Yilmaz, 2001):

- 788 1. The dip in a migrated section is greater than in the unmigrated section (migra-
789 tion *steepens* reflectors).
- 790 2. For areas of non-zero local dip the horizontal distance between points is shorter
791 after migration.
- 792 3. Migration moves events in an up-dip direction.

793 After Chun and Jacewitz (1981), for migrated dip α' , unmigrated dip α , local mi-
794 gration velocity, v , and TWTT t :

$$\begin{aligned}
\alpha' &= \frac{\alpha}{\sqrt{1 - \left(\frac{\alpha v(x,t)}{2}\right)^2}} \\
x' &= \frac{v(x,t)^2 t}{4} \alpha \\
t' &= t \left(1 - \sqrt{1 - \frac{\alpha v(x,t)}{2}}\right).
\end{aligned} \tag{A1}$$

795 We first solve for the un-migrated local dip value, $\alpha(x', t')$. Then we calculate the hor-
796 izontal and vertical (time) shift ($x' - x$ and $t' - t$). The de-migrated dip field $\alpha(x, t)$ is
797 estimated by applying image warping (with the horizontal and vertical shifts) to $\alpha(x', t')$.
798 The effect is to reverse the effect of migration on the dip field, to “de-migrate” the dip
799 field.

800 Acknowledgments

801 Pre-processed pre-stack seismic data, processing horizons, migration velocities and
802 code to reproduce the results using Madagascar (Fomel et al., 2013) are archived in Ford
803 (2020).

804 The authors wish to thank the crew, technicians and scientific party of the INSIGHT
805 cruises (Legs 1 and 2), particularly the onboard seismic processing team: R. Bartolomé,
806 P. Brito, A. Calahorrano and E. Piazza. Data for this study was collected in the frame-
807 work of the project INSIGHT (CTM2015-70155-R) funded by the Spanish “Ministerio
808 de Ciencia e Innovación” and the European Regional Development Fund. J. Ford was
809 supported by a Marie Curie Doctoral Fellowship through the SLATE Innovative Train-
810 ing Network within the European Union Framework Programme for Research and In-
811 novation Horizon 2020 under Grant Agreement No. 721403.

812 **References**

- 813 Alsop, G. I., & Marco, S. (2013, October). Seismogenic slump folds formed by
 814 gravity-driven tectonics down a negligible subaqueous slope. *Tectonophysics*,
 815 *605*, 48–69. doi: 10.1016/j.tecto.2013.04.004
- 816 Alves, T. M., Kurtev, K., Moore, G. F., & Strasser, M. (2014). Assessing the in-
 817 ternal character, reservoir potential, and seal competence of mass-transport
 818 deposits using seismic texture: A geophysical and petrophysical approach.
 819 *AAPG Bulletin*, *98*(4), 793–824. doi: 10.1306/09121313117
- 820 Badhani, S., Cattaneo, A., Collico, S., Urgeles, R., Dennielou, B., Leroux, E., . . .
 821 Droz, L. (2020). Integrated geophysical, sedimentological and geotechnical
 822 investigation of submarine landslides in the Gulf of Lions (Western Mediter-
 823 ranean). *Geological Society, London, Special Publications*, *500*(1), 359–376.
 824 doi: 10.1144/SP500-2019-175
- 825 Baptista, M., Heitor, S., Miranda, J., Miranda, P., & Victor, L. (1998). The 1755
 826 Lisbon tsunami; evaluation of the tsunami parameters. *Journal of Geodynam-
 827 ics*, *25*(1-2), 143–157. doi: 10.1016/S0264-3707(97)00019-7
- 828 Baptista, M., & Miranda, J. (2009). Revision of the Portuguese catalog of tsunamis.
 829 *Natural Hazards and Earth System Sciences*, *9*(1), 25–42. doi: 10.5194/nhess-9
 830 -25-2009
- 831 Berndt, C., Costa, S., Canals, M., Camerlenghi, A., de Mol, B., & Saunders,
 832 M. (2012, February). Repeated slope failure linked to fluid migration:
 833 The Ana submarine landslide complex, Eivissa Channel, Western Mediter-
 834 ranean Sea. *Earth and Planetary Science Letters*, *319-320*, 65–74. doi:
 835 10.1016/j.epsl.2011.11.045
- 836 Bhatnagar, P., Verma, S., & Bianco, R. (2019). Characterization of mass transport
 837 deposits using seismic attributes: Upper Leonard Formation, Permian Basin.
 838 *Interpretation*, *7*(4), SK19–SK32. doi: 10.1190/INT-2019-0036.1
- 839 Born, M., & Wolf, E. (1959). *Principles of optics: Electromagnetic theory of propa-
 840 gation, interference, and diffraction of light*. London Pergamon Press.
- 841 Brackenridge, R. E., Hernández-Molina, F. J., Stow, D. A. V., & Llave, E. (2013). A
 842 Pliocene mixed contourite–turbidite system offshore the Algarve Margin, Gulf
 843 of Cadiz: Seismic response, margin evolution and reservoir implications. *Ma-
 844 rine and Petroleum Geology*, *46*, 36–50. doi: 10.1016/j.marpetgeo.2013.05.015

- 845 Bull, S., Cartwright, J., & Huuse, M. (2009). A review of kinematic indicators from
846 mass-transport complexes using 3D seismic data. *Marine and Petroleum Geol-*
847 *ogy*, 26(7), 1132–1151. doi: 10.1016/j.marpetgeo.2008.09.011
- 848 Bull, S., & Cartwright, J. A. (2020). Line length balancing to evaluate multi-phase
849 submarine landslide development: an example from the Storegga Slide, Nor-
850 way. *Geological Society, London, Special Publications*, 500(1), 531–549. doi:
851 10.1144/SP500-2019-168
- 852 Cardona, S., Wood, L. J., Day-Stirrat, R. J., & Moscardelli, L. (2016). Fabric De-
853 velopment and Pore-Throat Reduction in a Mass-Transport Deposit in the
854 Jubilee Gas Field, Eastern Gulf of Mexico: Consequences for the Sealing Ca-
855 pacity of MTDs. In G. Lamarche et al. (Eds.), *Submarine Mass Movements*
856 *and their Consequences: 7th International Symposium* (pp. 27–37). Springer
857 International Publishing. doi: 10.1007/978-3-319-20979-1_3
- 858 Carter, L., Gavey, R., Talling, P., & Liu, J. (2014). Insights into Submarine Geohaz-
859 ards from Breaks in Subsea Telecommunication Cables. *Oceanography*, 27(2),
860 58–67. doi: 10.5670/oceanog.2014.40
- 861 Chen, J., & Schuster, G. T. (1999). Resolution limits of migrated images. *GEO-*
862 *PHYSICS*, 64(4), 1046–1053. doi: 10.1190/1.1444612
- 863 Chopra, S., & Marfurt, K. J. (2007). *Seismic Attributes for Prospect Identification*
864 *and Reservoir Characterization*. SEG Books.
- 865 Chun, J. H., & Jacewitz, C. A. (1981). Fundamentals of frequency domain migra-
866 tion. *GEOPHYSICS*, 46(5), 717–733. doi: 10.1190/1.1441211
- 867 Claerbout, J. F. (1992). *Earth Soundings Analysis: Processing Versus Inversion*.
868 Blackwell Scientific Publications.
- 869 Decker, L., Janson, X., & Fomel, S. (2015, February). Carbonate reservoir character-
870 ization using seismic diffraction imaging. *Interpretation*, 3(1), SF21–SF30. doi:
871 10.1190/INT-2014-0081.1
- 872 Decker, L., Merzlikin, D., & Fomel, S. (2017). Diffraction imaging and time-
873 migration velocity analysis using oriented velocity continuation. *GEO-*
874 *PHYSICS*, 82(2). doi: 10.1190/geo2016-0141.1
- 875 Dell, S., & Gajewski, D. (2011, September). Common-reflection-surface-based work-
876 flow for diffraction imaging. *GEOPHYSICS*, 76(5), S187–S195. doi: 10.1190/
877 geo2010-0229.1

- 878 Diviaco, P., Rebesco, M., & Camerlenghi, A. (2006). Late Pliocene Mega Debris
879 Flow Deposit and Related Fluid Escapes Identified on the Antarctic Peninsula
880 Continental Margin by Seismic Reflection Data Analysis. *Marine Geophysical
881 Researches*, *27*(2), 109–128. doi: 10.1007/s11001-005-3136-8
- 882 Fomel, S. (2002). Applications of plane-wave destruction filters. *GEOPHYSICS*,
883 *67*(6), 1946–1960. doi: 10.1190/1.1527095
- 884 Fomel, S., Landa, E., & Taner, M. (2007). Poststack velocity analysis by separa-
885 tion and imaging of seismic diffractions. *GEOPHYSICS*, *72*(6). doi: 10.1190/
886 1.2781533
- 887 Fomel, S., Sava, P., Vlad, I., Liu, Y., & Bashkardin, V. (2013). Madagascar: open-
888 source software project for multidimensional data analysis and reproducible
889 computational experiments. *Journal of Open Research Software*, *1*(1), e8. doi:
890 10.5334/jors.ag
- 891 Ford, J. (2020, October). *Multi-channel seismic reflection profiles MP06b and INS-
892 Line1 (INSIGHT cruises)*. Zenodo. (Dataset) doi: 10.5281/zenodo.3946170
- 893 Frey Martinez, J., Cartwright, J., & Hall, B. (2005). 3D seismic interpretation of
894 slump complexes: examples from the continental margin of Israel. *Basin Re-
895 search*, *17*(1), 83–108. doi: 10.1111/j.1365-2117.2005.00255.x
- 896 Gafeira, J., Long, D., Scrutton, R., & Evans, D. (2010, May). 3D seismic evidence
897 of internal structure within Tampen Slide deposits on the North Sea Fan:
898 are chaotic deposits that chaotic? *Journal of the Geological Society*, *167*(3),
899 605–616. doi: 10.1144/0016-76492009-047
- 900 Gazdag, J., & Sguazzero, P. (1984). Migration of seismic data by phase shift plus in-
901 terpolation. *Geophysics*, *49*(2), 124–131.
- 902 Gràcia, E., Vizcaino, A., Escutia, C., Asioli, A., Rodés, A., Pallàs, R., . . . Goldfin-
903 ger, C. (2010). Holocene earthquake record offshore Portugal (SW Iberia):
904 testing turbidite paleoseismology in a slow-convergence margin. *Quaternary
905 Science Reviews*, *29*(9-10), 1156–1172. doi: 10.1016/j.quascirev.2010.01.010
- 906 Gràcia, E., Dañobeitia, J., Vergés, J., Bartolomé, R., & Córdoba, D. (2003). Crustal
907 architecture and tectonic evolution of the Gulf of Cadiz (SW Iberian margin)
908 at the convergence of the Eurasian and African plates. *Tectonics*, *22*(4). doi:
909 10.1029/2001TC901045
- 910 Gràcia, E., Dañobeitia, J., Vergés, J., & Team, P. (2003). Mapping active

- 911 faults offshore Portugal (36N–38N): Implications for seismic hazard as-
 912 sessment along the southwest Iberian margin. *Geology*, *31*(1), 83. doi:
 913 10.1130/0091-7613(2003)031<0083:MAFOPN>2.0.CO;2
- 914 Gràcia, E., Urgeles, R., Rothenbeck, M., Wenzlaff, E., Steinführer, A., Kurbjuhn,
 915 T., ... INSIGHT Leg 1 cruise party (2018). *ImagiNg large SeismogenIc*
 916 *and tsunamiGenic structures of the Gulf of Cadiz with ultra-High resolution*
 917 *Technologies (INSIGHT) Leg 1 survey cruise report* (Tech. Rep.). Institut de
 918 Ciències del Mar - CSIC.
- 919 Harlan, W. S., Claerbout, J. F., & Rocca, F. (1984, November). Signal/noise separa-
 920 tion and velocity estimation. *GEOPHYSICS*, *49*(11), 1869–1880. doi: 10.1190/
 921 1.1441600
- 922 Karstens, J., Berndt, C., Urlaub, M., Watt, S. F., Micallef, A., Ray, M., ... Brune,
 923 S. (2019, July). From gradual spreading to catastrophic collapse – Reconstruc-
 924 tion of the 1888 Ritter Island volcanic sector collapse from high-resolution
 925 3D seismic data. *Earth and Planetary Science Letters*, *517*, 1–13. doi:
 926 10.1016/j.epsl.2019.04.009
- 927 Kessinger, W. (1992). Extended split-step Fourier migration. In *SEG Technical*
 928 *Program Expanded Abstracts 1992* (pp. 917–920). Society of Exploration Geo-
 929 physicists.
- 930 Khaidukov, V., Landa, E., & Moser, T. (2004). Diffraction imaging by focusing-
 931 defocusing: An outlook on seismic superresolution. *GEOPHYSICS*, *69*(6),
 932 1478–1490. doi: 10.1190/1.1836821
- 933 Klem-Musatov, K., Hoeber, H., Pelissier, M., & Moser, T. J. (Eds.). (2016).
 934 *Seismic Diffraction*. Society of Exploration Geophysicists. doi: 10.1190/
 935 1.9781560803188
- 936 Lackey, J., Moore, G., & Strasser, M. (2018, October). Three-dimensional map-
 937 ping and kinematic characterization of mass transport deposits along the outer
 938 Kumano Basin and Nankai accretionary wedge, southwest Japan. *Progress in*
 939 *Earth and Planetary Science*, *5*(1), 65. doi: 10.1186/s40645-018-0223-4
- 940 Leynaud, D., Mulder, T., Hanquiez, V., Gonthier, E., & Régert, A. (2017). Sediment
 941 failure types, preconditions and triggering factors in the Gulf of Cadiz. *Land-*
 942 *slides*, *14*(1), 233–248. doi: 10.1007/s10346-015-0674-2
- 943 Lo Iacono, C., Gràcia, E., Zaniboni, F., Pagnoni, G., Tinti, S., Bartolome, R., ...

- 944 Zitellini, N. (2012). Large, deepwater slope failures: Implications for landslide-
 945 generated tsunamis. *Geology*, *40*(10), 931–934. doi: 10.1130/G33446.1
- 946 Lucente, C. C., & Pini, G. A. (2003). Anatomy and emplacement mechanism of a
 947 large submarine slide within a Miocene foredeep in the northern Apennines,
 948 Italy: A field perspective. *American Journal of Science*, *303*(7), 565–602. doi:
 949 10.2475/ajs.303.7.565
- 950 Lumley, D. E., Claerbout, J. F., & Bevc, D. (1994). Anti-aliased Kirchhoff 3-D mi-
 951 gration. In *SEG Technical Program Expanded Abstracts 1994* (pp. 1282–1285).
 952 Society of Exploration Geophysicists. doi: 10.1190/1.1822760
- 953 Matias, L. M., Cunha, T., Annunziato, A., Baptista, M. A., & Carrilho, F. (2013).
 954 Tsunamigenic earthquakes in the Gulf of Cadiz: fault model and recur-
 955 rence. *Natural Hazards and Earth System Sciences*, *13*(1), 1–13. doi:
 956 10.5194/nhess-13-1-2013
- 957 Medialdea, T., Somoza, L., Pinheiro, L., Fernández-Puga, M., Vázquez, J., León, R.,
 958 ... Vegas, R. (2009). Tectonics and mud volcano development in the Gulf of
 959 Cádiz. *Marine Geology*, *261*(1-4), 48–63. doi: 10.1016/j.margeo.2008.10.007
- 960 Moser, T., & Howard, C. (2008). Diffraction imaging in depth. *Geophysical Prospect-*
 961 *ing*, *56*(5), 627–641. doi: 10.1111/j.1365-2478.2007.00718.x
- 962 Mulder, T., & Cochonat, P. (1996). Classification of offshore mass movements.
 963 *Journal of Sedimentary Research*, *66*(1), 43–57. doi: 10.1306/D42682AC-2B26
 964 -11D7-8648000102C1865D
- 965 Mulder, T., Gonthier, E., Lecroart, P., Hanquiez, V., Marches, E., & Voisset,
 966 M. (2009, May). Sediment failures and flows in the Gulf of Cadiz (east-
 967 ern Atlantic). *Marine and Petroleum Geology*, *26*(5), 660–672. doi:
 968 10.1016/j.marpetgeo.2008.02.009
- 969 Piper, D. J. W., Cochonat, P., & Morrison, M. L. (1999). The sequence of events
 970 around the epicentre of the 1929 Grand Banks earthquake: initiation of debris
 971 flows and turbidity current inferred from sidescan sonar. *Sedimentology*, *46*(1),
 972 79–97. doi: 10.1046/j.1365-3091.1999.00204.x
- 973 Piper, D. J. W., Pirmez, C., Manley, P. L., Long, D., Flood, R. D., Normark, W. R.,
 974 & Showers, W. (1997). Mass-transport deposits of the Amazon fan. *Proceed-*
 975 *ings of the Ocean Drilling Program. Scientific results*, *155*, 109–146.
- 976 Posamentier, H. W., & Martinsen, O. J. (2011). The Character and Genesis of Sub-

- 977 marine Mass-Transport Deposits: Insights from Outcrop and 3D Seismic Data.
 978 In R. C. Shipp, P. Weimer, & H. W. Posamentier (Eds.), *Mass-Transport De-*
 979 *posits in Deepwater Settings*. SEPM (Society for Sedimentary Geology). doi:
 980 10.2110/sepmsp.096
- 981 Preine, J., Schwarz, B., Bauer, A., & Hübscher, C. (2020). When There Is No
 982 Offset: A Demonstration of Seismic Diffraction Imaging and Depth-Velocity
 983 Model Building in the Southern Aegean Sea. *Journal of Geophysical Research:*
 984 *Solid Earth*, 125(9). doi: 10.1029/2020JB019961
- 985 Prior, D. B., Bornhold, B. D., & Johns, M. W. (1984). Depositional Characteristics
 986 of a Submarine Debris Flow. *The Journal of Geology*, 92(6), 707–727. doi: 10
 987 .1086/628907
- 988 Reshef, M., & Landa, E. (2009). Post-stack velocity analysis in the dip-angle do-
 989 main using diffractions. *Geophysical Prospecting*, 57(5), 811–821. doi: 10.1111/
 990 j.1365-2478.2008.00773.x
- 991 Satake, K. (2012). Tsunamis Generated by Submarine Landslides. In Y. Yamada et
 992 al. (Eds.), *Submarine Mass Movements and Their Consequences* (pp. 475–484).
 993 Dordrecht: Springer Netherlands. doi: 10.1007/978-94-007-2162-3_42
- 994 Sawyer, D. E., Flemings, P. B., Dugan, B., & Germaine, J. T. (2009). Retrogres-
 995 sive failures recorded in mass transport deposits in the Ursa Basin, Northern
 996 Gulf of Mexico. *Journal of Geophysical Research: Solid Earth*, 114(B10). doi:
 997 10.1029/2008JB006159
- 998 Schwarz, B. (2019a). Coherent wavefield subtraction for diffraction separation.
 999 *GEOPHYSICS*, 84(3), V157–V168. doi: 10.1190/geo2018-0368.1
- 1000 Schwarz, B. (2019b, January). An introduction to seismic diffraction. In
 1001 C. Schmelzbach (Ed.), *Advances in Geophysics* (Vol. 60, pp. 1–64). Elsevier.
 1002 doi: 10.1016/bs.agph.2019.05.001
- 1003 Schwarz, B., & Gajewski, D. (2017, October). Accessing the diffracted wavefield by
 1004 coherent subtraction. *Geophysical Journal International*, 211(1), 45–49. (Pub-
 1005 lisher: Oxford Academic) doi: 10.1093/gji/ggx291
- 1006 Shipp, R. C., Nott, J. A., & Newlin, J. A. (2004). Physical Characteristics and
 1007 Impact of Mass Transport Complexes on Deepwater Jetted Conductors and
 1008 Suction Anchor Piles. In *Offshore Technology Conference*. Houston, Texas:
 1009 Offshore Technology Conference. doi: 10.4043/16751-MS

- 1010 Silva, P., Roque, C., Drago, T., Belén, A., Henry, B., Gemma, E., . . . Vázquez,
 1011 J. (2020, February). Multidisciplinary characterization of Quaternary mass
 1012 movement deposits in the Portimão Bank (Gulf of Cadiz, SW Iberia). *Marine*
 1013 *Geology*, *420*, 106086. doi: 10.1016/j.margeo.2019.106086
- 1014 Sobiesiak, M. S., Kneller, B., Alsop, G. I., & Milana, J. P. (2016, October). Internal
 1015 deformation and kinematic indicators within a tripartite mass transport de-
 1016 posit, NW Argentina. *Sedimentary Geology*, *344*(Supplement C), 364–381. doi:
 1017 10.1016/j.sedgeo.2016.04.006
- 1018 Steventon, M. J., Jackson, C. A.-L., Hodgson, D. M., & Johnson, H. D. (2019).
 1019 Strain analysis of a seismically imaged mass-transport complex, offshore
 1020 Uruguay. *Basin Research*, *31*(3), 600–620. doi: 10.1111/bre.12337
- 1021 Stolt, R. H. (1978). Migration by Fourier transform. *GEOPHYSICS*, *43*(1), 23–48.
 1022 doi: 10.1190/1.1440826
- 1023 Talling, P. J., Wynn, R. B., Schmitt, D. N., Rixon, R., Sumner, E., & Amy, L.
 1024 (2010, October). How Did Thin Submarine Debris Flows Carry Boulder-Sized
 1025 Intraclasts for Remarkable Distances Across Low Gradients to the Far Reaches
 1026 of the Mississippi Fan? *Journal of Sedimentary Research*, *80*(10), 829–851.
 1027 doi: 10.2110/jsr.2010.076
- 1028 Taner, M., Fomel, S., & Landa, E. (2006, January). Separation and imaging of seis-
 1029 mic diffractions using plane-wave decomposition. In *SEG Technical Program*
 1030 *Expanded Abstracts 2006* (pp. 2401–2405). Society of Exploration Geophysi-
 1031 cists. doi: 10.1190/1.2370017
- 1032 Tappin, D. R., Watts, P., McMurtry, G. M., Lafoy, Y., & Matsumoto, T. (2001).
 1033 The Sissano, Papua New Guinea tsunami of July 1998 — offshore evi-
 1034 dence on the source mechanism. *Marine Geology*, *175*(1), 1–23. doi:
 1035 10.1016/S0025-3227(01)00131-1
- 1036 Terrinha, P., Pinheiro, L., Henriot, J.-P., Matias, L., Ivanov, M., Monteiro, J., . . .
 1037 Rovere, M. (2003). Tsunamigenic-seismogenic structures, neotectonics, sedi-
 1038 mentary processes and slope instability on the southwest Portuguese Margin.
 1039 *Marine Geology*, *195*(1-4), 55–73. doi: 10.1016/S0025-3227(02)00682-5
- 1040 Urgeles, R., & Camerlenghi, A. (2013). Submarine landslides of the Mediterranean
 1041 Sea: Trigger mechanisms, dynamics, and frequency-magnitude distribution.
 1042 *Journal of Geophysical Research: Earth Surface*, *118*(4), 2013JF002720. doi:

- 1043 10.1002/2013JF002720
- 1044 Urgeles, R., INSIGHT Leg 2 cruise shipboard participants, & . (2019). *ImagiNg*
1045 *large SeismogenIc and tsunamiGenic structures of the Gulf of Cadiz with ultra-*
1046 *High resolution Technologies (INSIGHT) Leg 2 survey cruise report* (Tech.
1047 Rep.). Institute of Marine Sciences, Barcelona.
- 1048 Urgeles, R., Masson, D. G., Canals, M., Watts, A. B., & Bas, T. L. (1999). Re-
1049 current large-scale landsliding on the west flank of La Palma, Canary Islands.
1050 *Journal of Geophysical Research: Solid Earth*, *104*(B11), 25331–25348. doi:
1051 <https://doi.org/10.1029/1999JB900243>
- 1052 Vizcaino, A., Gràcia, E., Pallàs, R., Garcia-Orellana, J., Casas, D., Willmott, V., ...
1053 Asioli, A. (2006). Sedimentology, physical properties and age of mass transport
1054 deposits associated with the Marquês de Pombal Fault, Southwest Portuguese
1055 Margin. *Norwegian Journal of Geology*, *10*.
- 1056 Weimer, P., & Shipp, C. (2004). Mass Transport Complex: Musing on Past Uses
1057 and Suggestions for Future Directions. In *Offshore Technology Conference*.
1058 Houston, Texas: Offshore Technology Conference. doi: 10.4043/16752-MS
- 1059 Yilmaz, O. (2001). *Seismic Data Analysis: Processing, Inversion, and Interpretation*
1060 *of Seismic Data* (2Volume Set edition ed.). Tulsa, OK: Society of Exploration
1061 Geophysicists.
- 1062 Zitellini, N., Gràcia, E., Matias, L., Terrinha, P., Abreu, M., DeAlteriis, G., ... Mul-
1063 der, T. (2009). The quest for the Africa–Eurasia plate boundary west of the
1064 Strait of Gibraltar. *Earth and Planetary Science Letters*, *280*(1-4), 13–50. doi:
1065 10.1016/j.epsl.2008.12.005
- 1066 Zitellini, N., Rovere, M., Terrinha, P., Chierici, F., & Matias, L. (2004). Neo-
1067 gene Through Quaternary Tectonic Reactivation of SW Iberian Passive
1068 Margin. *Pure and Applied Geophysics*, *161*(3), 565–587. doi: 10.1007/
1069 s00024-003-2463-4